INTERNATIONAL ATOMIC ENERGY AGENCY
UNITED NATIONS EDUCATIONAL, SCIENTIFIC AND CULTURAL ORGANIZATION
INTERNATIONAL CENTRE FOR THEORETICAL PHYSICS
I.C.T.P., P.O. BOX 586, 34100 TRIESTE, ITALY. CABLE CENTRATOM TRIESTE

SMR/406-3

THIRD AUTUMN WORKSHOP ON ATMOSPHERIC
RADIATION AND CLOUD PHYSICS
27 November - 15 December 1989

"Measurement of Cloud Parameters Using AVHRR"

Karl Theodor KRIEBEL
Institut für Physik der Atmosphäre DFVLR
Wessling
Federal Republic of Germany

Please note: These are preliminary notes intended for internal distribution only.

ICTP Workshop on Atmospheric Radiation and Cloud Physics 1989

MEASUREMENT OF CLOUD PARAMETERS USING AVHRR

K.T. Kriebel
Deutsche Forschungsanstalt für Luft- und Raumfahrt
8031 Oberpfaffenhofen, FRG

1. INTRODUCTION
   Measurement: Remote Sensing Technique
   Cloud Parameters: Cloud analysis to obtain optical properties
   AVHRR: Satellite system, satellite data
2. REMOTE SENSING TECHNIQUE
   Definitions, principles, use of RTE
   Surface data: Cloud contamination, atmospheric correction
   Cloud data: Broken clouds, atmospheric correction above clouds
3. AVHRR
   NOAA satellite system
   AVHRR scanner
   Multispectral prospects: MSG, AVHRR/3, AMRIR
4. APOLLO
   Calibration, navigation
   Cloud mask: 3 pixel groups cloud free, fully cloudy,
   partially cloudy = Cloud Detection
   Cloud coverage = Cloud Classification
   Surface Properties
   Cloud optical properties = Cloud Analysis
5. CONCLUSIONS

1. INTRODUCTION

The title of this talk gives rise to three chapters. Firstly, 'measurement' implies the use of remote sensing techniques, because we restrict ourselves to satellite data. Therefore, chapter 2 deals with the definition and the principles of remote sensing, based on the equation of radiative transfer (RTE), and with the sources of error if physical quantities are to be extracted from measured data. Particular emphasis is put on the correction of atmospheric effects.
Secondly, the 'Advanced Very High Resolution Radiometer' (AVHRR) which is onboard the NOAA satellites, will be used as the data source. Therefore in chapter 3 the necessary information is given on the TIROS-N/NOAA satellite system and its imager, the AVHRR. Future developments of such scanning instruments will be discussed. Finally, 'cloud parameters' refers to bulk optical properties which are related by parametrization schemes to radiative quantities which can be measured by remote sensing. Chapter 4 deals with the possibilities of processing multispectral satellite data. Based on the APOLLO algorithm package, it is demonstrated how AVHRR data can be used to

a) detect clouds, i.e. to arrive at three groups of cloud free, fully cloudy and partially cloudy pixels,
b) classify clouds, i.e. to obtain cloud coverage for different cloud types,
c) analyse clouds, i.e. to obtain cloud optical properties.

The derivation of surface data like albedo or vegetation index is not part of this talk. It will be mentioned as far as it is required for tje cloud analysis.

2. REMOTE SENSING TECHNIQUE

2. Principles of Remote Sensing

2.1. Definition of Remote Sensing

In general, remote sensing can be defined as follows: From the state of a field at one location conclusions are drawn about quantities that had an effect on the field at a different location. So far, nothing has been said about the nature of the field. Here we will deliberately restrict ourselves to extracting information carried by electromagnetic waves and will exclude acoustic and radioactive waves as information carriers.

So a necessary condition for remote sensing is therefore an interaction between the electromagnetic field and the matter whose properties are to be determined. As we saw in the previous lecture, speaking strictly, there are only two interactions between electromagnetic radiation and matter, namely absorption and emission. They are, however, usefully regrouped into four classes of interaction processes: scattering, reflection, absorption and emission. Here absorption means the permanent loss of a photon from the radiation field, while the temporary, usually very brief, removal of a photon from the radiation field by absorption and spontaneous re-emission is called either scattering or reflection.

These interaction processes alone determine the strength of the directly measured quantity, the radiation field, and are what have to be deduced from the measurements. Now taking for example the atmosphere, optical depth and scattering function are not determined by just one substance but by a mixture of differing substances. This means it is not in principle possible to determine from a single measurement the properties of one substance, instead one obtains the properties of a mixture of substances. To split the measured properties of the mixture into information about the constituents of the mixture is an inversion problem and generally gives rise to ambiguities. In practice, modelling assumptions and/or additional measurements are made to get a unique connection between the property of a component of the mixture which one wants to know and the actual quantity measured. An example of the use of modelling assumptions is aerosol measurement, where the fraction of Rayleigh scattering known by a priori knowledge (the Rayleigh optical depth is nearly constant because of the small relative variation of the barometric pressure) is subtracted from the measurement leaving the aerosol's contribution. An

example of using additional measurements is the DIAL technique where measurements are made simultaneously at two distinct, cleverly chosen wavelengths. This will be discussed in more detail in the next lecture.

Having solved the problem of getting a unique result from the initial ambiguity, more interpretation is often needed because what one wants to know about a substance often is not identical with the quantity that directly influences the measurable radiation field. An example is the determination of the aerosol mass which is only possible when additional information is available, namely the aerosol size distribution and the complex refractive index of the aerosol particles. This additional information can be taken from modelling assumptions or from additional measurements (or a suitable combination of the two). The achieved result is generally more accurate if additional measurements are used rather than assumptions. In our example, additional measurements can consist in measuring the aerosol scattering not at one wavelength but at several. So we see that it is crucial to remote sensing to establish the quantitative connection between measurable quantity and required quantity. Generally this is done with the help of computer modelling, that is the radiative transfer equation (RTE) is used to calculate the radiation field in the atmosphere which can in turn be used to separately determine the influence of each quantity on the radiation field.

This tells one the possible accuracy of the required quantity as determined by the accuracy of the measured quantity and the accuracy with which the perturbing quantities are known. Such sensitivity studies can generally only be carried out by computer modelling, and not by using measurements of the real atmosphere because it practically never happens that just one property of the atmosphere changes alone, instead several properties change simultaneously.

2.2. Basic Measurement Schemes

The four possible interaction processes between radiation and matter are, as has already been stated, scattering, absorption, reflection and emission. Figure 2.2.1 shows the possible geometric configurations which can be used for remote sensing. It is clear that scattering, reflection and emission can be measured on their own, while at least in the solar spectral region, absorption can only be measured together with scattering as

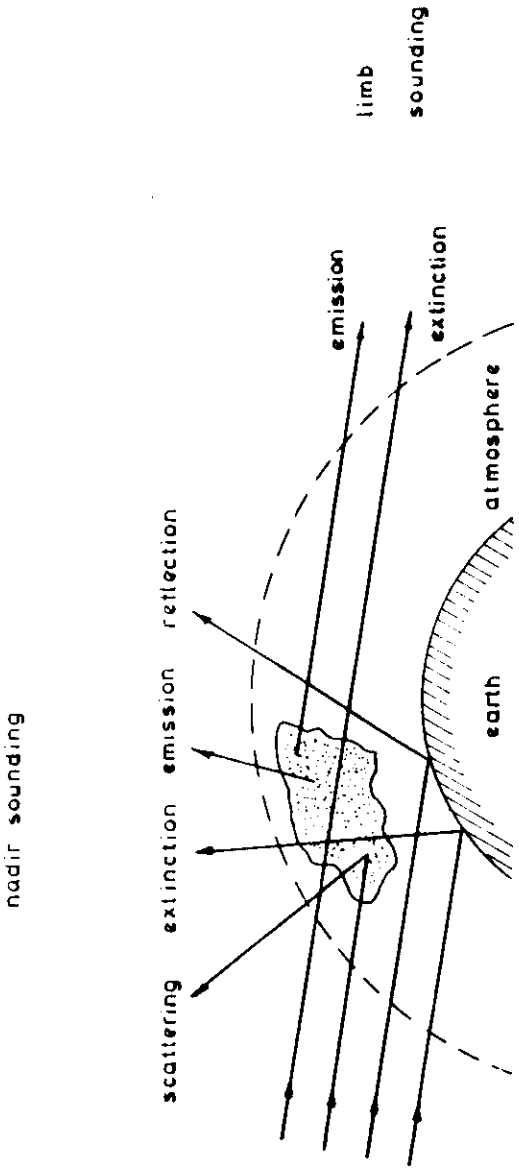

Fig. 2.1 Geometries of possible interactions between radiation and matter

extinction. Note that the figure only shows configurations in which both the source and the detector are outside the atmosphere, and does not consider cases where one or both are inside the atmosphere or on the ground. If this were the case, the principles that apply to the measurement geometry would not in fact differ.

If we use the radiation from natural sources as the information carrier then we speak of passive methods. If artificial sources e.g. Lasers are used, then we speak of active methods. It is also useful to distinguish between solar (shortwave) and terrestrial (longwave) spectral regions even though the boundary is a little fuzzy, it lies between 3 and 5 µm wavelength. The following table summarizes the possible measurement schemes, ordered by whether they use the short or long wave regions, are active or passive, and by the type of interaction used.

Spectral Region	Mode	Usable Interaction Processes
shortwave	passive	scattering, reflection, extinction (absorption)
shortwave	active	scattering, reflection, extinction (absorption)
longwave	passive	emission, absorption (extinction)
longwave	active	scattering, reflection, extinction (absorption)

Which of these conceivable schemes are to be used in practice? A few typical examples are:

Shortwave passive methods: scattering is used by Koepke to determine turbidity (this will be explained later); reflection is used by Kriebel to obtain reflection functions; extinction is used by the occultation method on board SAM II for the measurement of stratospheric aerosols and is also used by ground based sun photometer measurements. It makes no sense to apply the solar occultation method to the troposphere because of the ever-present clc

Shortwave active methods: Scattering is used to measure aerosols using LIDAR-techniques, reflection in conjunction with extinction is used for measuring aerosols using the LPA technique and extinction is used for measuring trace gases using the DIAL method.

Longwave passive methods: Emission and absorption are used for measuring trace gases with gas correlation radiometers and Laser heterodyne detection.

Longwave active methods: These are the same as the shortwave active methods.

Insert pages 34-40

2.3. Adaptation of the RTE to RS Measurement Schemes

In this chapter the equations needed for RS measurements are derived from the RTE, whose various terms were listed in chapter 1.8.3.

Terms 1, 2, 5 and 6 of the upwelling radiance are needed for shortwave passive methods that use scattered sunlight.

When measuring through the atmosphere against the sun (e.g. solar occultation and sun photometer) term 7 of the downwelling radiance becomes crucial, and all the others can be excluded. Terms 3 and 4 of the upwelling radiance are what is needed for longwave passive methods.

Shortwave and longwave active methods do not differ and can be treated together.

The LPA without reflecting target needs a remote detector to measure the extinction of the laser radiation and so it has an equivalent geometry to the solar occultation method. Here too, term 7 of the downwelling radiance is the important one.

The LPA method with a reflecting target detects radiation emitted by a laser after it has traveled through the atmosphere to a target (e.g. retroreflector, earth's surface), has been reflected there and has returned along the same path through the atmosphere to the detector which is usually directly adjacent to the laser. This configuration must therefore be describable by term 5 of the RTE for upwelling radiance. The LIDAR equa-

tion will be derived from it, as follows. The RTE using term 5 alone has the form

$$L_\lambda(\tau_\lambda,\mu,\varphi) = \gamma_\lambda(\mu,\varphi;\mu_o',\varphi_o')\ E_\lambda^o \mu_o'\ e^{-\frac{a_{E\lambda}}{\mu_o'}}\ e^{-\frac{a_{E\lambda}-\tau_\lambda}{\mu}}$$

If we imagine the laser and detector are on board a satellite, that is outside the atmosphere, and replace the solar radiation E_λ^o by the laser radiation E_λ^L and call the direction of the laser beam $(-\mu_o', \varphi_o')$, the reflection direction (μ_o, φ_o), then we get

$$L_\lambda(0,\mu_o,\varphi_o) = \gamma_\lambda(\mu_o,\varphi_o;\mu_o',\varphi_o')\ E_\lambda^L\ \mu_o'\ e^{-2a_{E\lambda}/\mu_o}$$

This is already the LIDAR equation, but not in its usual form. To get that, we multiply both sides by A Ω, where A is the receiver surface and Ω is the solid angle subtended by the laser beam that is $\Omega = F/R^2$ where F = illuminated area perpendicular to the direction of propagation and R = distance from the transmitter/receiver to the target. This gives rise to

$$L_\lambda(0,\mu_o,\varphi_o)\ A\Omega = \gamma_\lambda(\mu_o,\varphi_o;\mu_o',\varphi_o')\ E_\lambda^L\ \mu_o\ e^{-2a_{E\lambda}/\mu_o}\ \frac{A}{R^2}\ F$$

Now $L_\lambda(0,\mu_o, \varphi_o)\ A\Omega = P_\lambda(R)$ which is the reflected or backscattered power; $E_\lambda^L\ F\mu_o = P_{o\lambda}$ which is what the laser emits, the so called transmitted power, where $\mu_o = 1$ since the illumination is perpendicular to the target F. From that,

$$P_\lambda(R) = \gamma_\lambda(\mu_o,\varphi_o;\mu_o',\varphi_o')\ P_{o\lambda}\ \frac{A}{R^2}\ e^{-2a_{E\lambda}}$$

Just replacing $P_\lambda(R)$ by the received power $P_{r\lambda}(R)$ where $P_\lambda(R) = K^{-1}P_{r\lambda}(R)$ and K = optical systems efficiency and replacing the reflection function γ_λ by the reflectance factor $\rho_\lambda = \pi\ \gamma_\lambda$, gives

$$P_{r\lambda}(R) = \frac{\rho_\lambda}{\pi}\ K\ P_{o\lambda}\ \frac{A}{R^2}\ \exp(-2a_{E\lambda})$$

or with

$$a_{E\lambda} = \int_o^R \alpha_\lambda(r)dr$$

$$P_{r\lambda}(R) = \frac{\rho_\lambda}{\pi}\ K\ P_{o\lambda}\ \frac{A}{R^2}\ \exp(-2\int_o^R \alpha_\lambda(r)dr$$

This form of the LIDAR equation appears in every handbook of LIDAR techniques for the LPA method with a reflecting target, that is for non-range- resolved methods.

With range resolved methods the laser beam is reflected at the air-aerosol mixture where, all according to the time constant, different sized range cells with length ΔR are resolved. In this instance we are not interested in the radiation that traveled via the reflector or the earth's surface but in the radiation scattered from the direct beam as described in term 2 of the RTE for upwelling radiance.

Here the laser signals also travel through the atmosphere twice but not all the way through it, but only to the range cells of interest and back. The RTE with term 2 is

$$L_\lambda(\tau_\lambda,\mu,\varphi) = \int_{\tau_\lambda}^{a_{E\lambda}} E_\lambda^o\ e^{-t_\lambda/\mu_o'}\ (1-k_\lambda)\ \frac{P_\lambda'}{4\pi}(\mu,\varphi;-\mu_o',\varphi_o')\ e^{-\frac{t_\lambda-\tau_\lambda}{\mu}}\ \frac{dt_\lambda}{\mu}$$

Again we replace E_λ^o by E_λ^L, consider the direction (μ_o, φ_o) and imagine the detector to be above the atmosphere:

$$L_\lambda(0,\mu_o,\varphi_o) = \int_o^{a_{E\lambda}} E_\lambda^L\ e^{-t_\lambda/\mu_o'}\ (1-k_\lambda)\ \frac{P_\lambda'}{4\pi}(\mu_o,\varphi_o;-\mu_o',\varphi_o')\ e^{-t_\lambda/\mu_o}\ \frac{dt_\lambda}{\mu_o}$$

Since we want range resolved information, we ignore the integral from $a_{E\lambda}$ to 0 and instead consider the path ΔR along the range cell, which makes us write dt_λ as $\Delta\tau_\lambda$. $\tau_\lambda(R)$ represents the optical depth of the atmosphere from the top to the relevant range cell. This gives rise to

$$L_\lambda(0,\mu_o,\varphi_o) = E_\lambda^L\ e^{-\tau_\lambda(R)/\mu_o'}\ (1-k_\lambda)\ \frac{P_\lambda'}{4\pi}(\mu_o,\varphi_o;-\mu_o',\varphi_o')\ e^{-\tau_\lambda(R)/\mu_o}\ \frac{\Delta\tau_\lambda}{\mu_o}$$

or since $\mu_o' = \mu_o$

$$L_\lambda(0,\mu_o,\varphi_o) = (1-k_\lambda)\,\frac{P'_\lambda}{4\pi}(\mu_o,\varphi_o;-\mu_o,\varphi_o)\,\frac{\Delta\tau_\lambda}{\mu_o}\,E^L_\lambda\,e^{-2\tau_\lambda(R)/\mu_o}$$

At the scattering volume $1-k_\lambda = \dfrac{\alpha_{s\lambda}}{\alpha_\lambda}$ with $\Delta\tau_\lambda = \alpha_\lambda \Delta R$

Since ΔR lies in the direction of propagation, $\mu_o = 1$, that is the volume is illuminated perpendicularly. This gives

$$L_\lambda(0,\mu_o,\varphi_o) = \frac{\alpha_{s\lambda}}{\alpha_\lambda}\,\frac{P'_\lambda}{4\pi}\,(\mu_o,\varphi_o;-\mu_o,\varphi_o)\alpha_\lambda\,\Delta R\,E^L_\lambda\,e^{-2\tau_\lambda(R)}$$

Now $$\alpha_{s\lambda}\,P'_\lambda(\mu_o,\varphi_o;-\mu_o,\varphi_o) = \beta_\lambda$$

and with β_λ = the value of the absolute scattering function at a scattering angle of 180°, the so-called backscatter coefficient, we get

$$L_\lambda(0,\mu_o,\varphi_o) = \frac{\beta_\lambda}{4\pi}\,\Delta R\,E^L_\lambda\,e^{-2\tau_\lambda(R)}$$

This equation is changed into the usual from, analogously to the way it was done for the LPA method:

$$P_{r\lambda}(R) = \frac{\beta_\lambda}{4\pi}\,\Delta R\,K\,P_{o\lambda}\,\frac{A}{R^2}\,\exp\left(-2\int_o^R \alpha_\lambda(r)dr\right)$$

with the difference that R now stands for the distance from transmitter/receiver to the range cell, and not as with the LPA method, the distance to the ground.

These two Lidar equations completely describe the backscattered or reflected laser signal. Nevertheless when using shortwave measuring methods one must also remember that during the day the radiation field is not solely determined by the laser signal; the scattered solar radiation also makes a contribution. This is described by terms 1, 2, 5 and 6 of the RTE for upwelling radiance, and must be taken into account unless one considers it to be negligible in comparison to the scattered laser radiation. This depends, for instance, on the wavelength and power of the laser.

Now the RTE can be written in the following form

$$\mu\,\frac{dL_\lambda}{d\tau_\lambda} = -L_\lambda + J^{dif}_\lambda + J^{dir}_\lambda + J^c_\lambda$$

or, in more detail

$$\mu\,\frac{dL_\lambda(\tau_\lambda,\mu,\varphi)}{d\tau_\lambda} = -L_\lambda(\tau_\lambda,\mu,\varphi)$$

$$+(1-k_\lambda)\int_o^{2\pi}\int_{-1}^{+1}\frac{P'_\lambda}{4\pi}(\mu,\varphi;\mu',\varphi')L_\lambda(\tau_\lambda,\mu',\varphi')\,d\mu'd\varphi'$$

$$+(1-k_\lambda)\,\frac{P'_\lambda}{4\pi}(\mu,\varphi;-\mu_o',\varphi_o')\,E^o_\lambda\,e^{-\tau_\lambda/\mu_o}$$

$$+\,k_\lambda\,B_\lambda(T)$$

According to the derivation, we have here a one dimensional model, that is the atmosphere is horizontally homogeneous at each level, and extends out to infinity. For practical purposes a horizontal homogeneity of 30 km is sufficient. We have a plane, not a curved, atmosphere. In practice this means that elevation angles of less than 3° to 5° cannot be properly handled. There is only one extraterrestrial source (the sun) and so the strength of the incoming radiation is the same all across the horizontal plane. The scattering behaviour of the particles is axially symmetrical about the direction of the incident beam so that the scattering function only has one independent variable, the scattering angle Θ. The radiative transfer equation only holds for the monochromatic case, that is when at the wavelength in question the optical effects of the atmosphere can be described by an optical thickness; then transmission functions are exponential functions. Section 1.8.3 will show how it is still possible to write the radiative transfer equation for absorption bands in which the optical effects at one wavelength cannot be described by just one optical depth.

Our version of the RTE holds for the radiances without considering the polarization of the radiation. If one wants to take it into account then the RTE must be applied separately to each of the four Stokes parameters which describe the radiation field including the polarization. We have

not done so as it would make the presentation unnecessarily tortuous. It should be stressed though, that all the remarks that follow will hold as if not only the strength of the radiation field had been taken into account but also the degree and the plane of polarization.

The RTE is a tool to accurately calculate the complete radiation field in the atmosphere.

However, it is an integro-differential equation because the term to the left of the equals sign contains a derivative of the radiation field, the first term to the right of the equals sign contains the radiation field itself and the second term to the right of the equals sign contains the radiation field as an integrand.

It can only be solved numerically and this is only possible if one does not use its differential form but its integral form (introduced in the next section) which includes the boundary conditions.

1.8.3 The Radiative Transfer Equation in Integral Form

By formally solving the differential RTE

$$\mu \frac{dL_\lambda(\tau_\lambda,\mu,\varphi)}{d\tau_\lambda} = - L_\lambda(\tau_\lambda,\mu,\varphi) + J_\lambda(\tau_\lambda,\mu,\varphi)$$

and separating the radiance into the upwelling and downwelling components, we get the integral form of the RTE

upwelling:

$$L_\lambda(\tau_\lambda,\mu,\varphi) = L_\lambda(a_{E\lambda},\mu,\varphi)\, e^{-\frac{a_{E\lambda}-\tau_\lambda}{\mu}} + \int_{\tau_\lambda}^{a_{E\lambda}} J_\lambda(t_\lambda,\mu,\varphi) e^{-\frac{t_\lambda-\tau_\lambda}{\mu}} \frac{dt_\lambda}{\mu}$$

with $0 < \mu \leq 1$

downwelling:

$$L_\lambda(\tau_\lambda,-\mu,\varphi) = L_\lambda(0,-\mu,\varphi) e^{-\tau_\lambda/\mu} + \int_0^{\tau_\lambda} J_\lambda(t_\lambda,-\mu,\varphi) e^{-\frac{\tau_\lambda-t_\lambda}{\mu}} \frac{dt_\lambda}{\mu}$$

with $0 < \mu \leq 1$

Since we are concerned with a one-dimensional model there is just an upper and a lower boundary condition, and no lateral ones.

At the top of the atmosphere (τ_λ=0) only solar radiation enters, so

$$L_\lambda(0,-\mu,\varphi) = L_\lambda^o(-\mu_o',\varphi_o')\, \delta(-\mu,-\mu_o')\, \delta(\varphi,\varphi_o')$$

The Dirac delta functions ensure that this term is zero except for the direction of sun (μ_o', φ_o').

The bottom of the atmosphere, the earth's surface is described by its angle dependent reflection function and by its thermal emission, which is given by the Planck function with the temperature of the earth's surface $B_\lambda(T_S)$, multiplied by its spectral emittance $\varepsilon_\lambda = k_{\lambda S}$
where $0 \leq \varepsilon_\lambda \leq 1$.

The irradiation of the earth's surface results from the direct solar radiation and the scattered radiation from all over the sky

$$E_\lambda(a_{E\lambda}) = E_\lambda^o\, \mu_o'\, e^{-a_{E\lambda}/\mu_o'} + \int_0^{2\pi}\int_0^1 L_\lambda(a_{E\lambda},-\mu',\varphi')\, \mu' d\mu' d\varphi'$$

and hence

$$L_\lambda(a_{E\lambda},\mu,\varphi) = Y_\lambda(\mu,\varphi;\mu_o',\varphi_o')\, E_\lambda^o\, \mu_o'\, e^{-a_{E\lambda}/\mu_o'} + \int_0^{2\pi}\int_0^1 Y_\lambda(\mu,\varphi;\mu',\varphi')\, L_\lambda(a_{E\lambda},-\mu',\varphi')\mu' d\mu' d\varphi' + \varepsilon_\lambda\, B_\lambda(T_S)$$

If one inserts the boundary conditions and the source functions into the integral form of the RTE, it yields the following complete form of the radiative transfer equation:

upwelling radiances:

$$\text{(term 0)} \quad L_\lambda(\tau_\lambda,\mu,\varphi) =$$

$$\text{(term 1)} \quad \int_{\tau_\lambda}^{a_{E\lambda}} (1-k_\lambda) \int_0^{2\pi} \int_{-1}^{+1} \frac{P'_\lambda}{4\pi}(\mu,\varphi;\mu',\varphi') L_\lambda(\tau_\lambda,\mu',\varphi')\, d\mu' d\varphi'\, e^{-\frac{t_\lambda-\tau_\lambda}{\mu}} \frac{dt_\lambda}{\mu}$$

$$\text{(term 2)} + \int_{\tau_\lambda}^{a_{E\lambda}} E^o_\lambda\, e^{-t_\lambda/\mu'_o} (1-k_\lambda) \frac{P'_\lambda}{4\pi}(\mu,\varphi;-\mu'_o,\varphi'_o)\, e^{-\frac{t_\lambda-\tau_\lambda}{\mu}} \frac{dt_\lambda}{\mu}$$

$$\text{(term 3)} + \int_{\tau_\lambda}^{a_{E\lambda}} k_\lambda\, B_\lambda(T(t_\lambda))\, e^{-\frac{t_\lambda-\tau_\lambda}{\mu}} \frac{dt_\lambda}{\mu}$$

$$\text{(term 4)} + \varepsilon_\lambda\, B_\lambda(T_s)\, e^{-\frac{a_{E\lambda}-\tau_\lambda}{\mu}}$$

$$\text{(term 5)} + \gamma_\lambda(\mu,\varphi;\mu'_o,\varphi'_o)\, E^o_\lambda \mu'_o\, e^{-\frac{a_{E\lambda}}{\mu'_o}}\, e^{-\frac{a_{E\lambda}-\tau_\lambda}{\mu}}$$

$$\text{(term 6)} + \int_0^{2\pi} \int_0^{1} \gamma_\lambda(\mu,\varphi;\mu',\varphi')\, L_\lambda(a_{E\lambda},-\mu',\varphi')\mu' d\mu' d\varphi' e^{-\frac{a_{E\lambda}-\tau_\lambda}{\mu}}$$

with $0 < \mu \leq 1$

downwelling radiances:

$$\text{(term 0)} \quad L_\lambda(\tau_\lambda,-\mu,\varphi) =$$

$$\text{(term 1)} \quad \int_0^{\tau_\lambda} (1-k_\lambda) \int_0^{2\pi} \int_{-1}^{+1} \frac{P'_\lambda}{4\pi}(-\mu,\varphi;\mu',\varphi') L_\lambda(t_\lambda,\mu',\varphi') d\mu' d\varphi' e^{-\frac{\tau_\lambda-t_\lambda}{\mu}} \frac{dt_\lambda}{\mu}$$

$$\text{(term 2)} + \int_0^{\tau_\lambda} E^o_\lambda\, e^{-t_\lambda/\mu'_o} (1-k_\lambda) \frac{P'_\lambda}{4\pi}(-\mu,\varphi;-\mu'_o,\varphi'_o)\, e^{-\frac{\tau_\lambda-t_\lambda}{\mu}} \frac{dt_\lambda}{\mu}$$

$$\text{(term 3)} + \int_0^{\tau_\lambda} k_\lambda\, B_\lambda(T(t_\lambda))\, e^{-\frac{\tau_\lambda-t_\lambda}{\mu}} \frac{dt_\lambda}{\mu}$$

$$\text{(term 7)} + L^o_\lambda(-\mu'_o,\varphi'_o)\, \delta(-\mu,-\mu'_o)\, \delta(\varphi,\varphi'_o)\, e^{-\frac{\tau_\lambda}{\mu}}$$

with $0 < \mu \leq 1$

Let us now consider, in order, the individual terms of both parts of the RTE. Considering first the upwelling radiance, left of the equals sign we have written the radiance at a particular level τ_λ going in direction (μ,φ). To the right of the equals sign there is written in:

Term 1: The contribution to the radiation from all the photons which are scattered in direction (μ,φ) somewhere between the ground and level τ_λ without having interacted with the ground and which are attenuated according to the law of extinction on their way back to level τ_λ except for the photons which are scattered out of the direct solar beam into direction (μ,φ).

Term 2: The contribution of those photons that are scattered out of the direct solar beam into direction (μ,φ) somewhere between the ground and level τ_λ and that are attenuated on their way to level τ_λ.

Term 3+4: The contribution of the thermal photons emitted from the ground and along the path from the ground into direction (μ,φ) up to level τ_λ, which are also attenuated along this path.

Term 5: The contribution of the direct solar beam from direction $(-\mu_0',\varphi_0')$ which is attenuated on its way down through the atmosphere, is reflected at the ground into direction (μ,φ) and is again attenuated on its way from the ground to level τ_λ.

Term 6: The contribution of the diffuse radiation from the sky which is reflected at the ground into direction (μ,φ) and which is attenuated on its way from the ground to level τ_λ.

The RTE for the downwelling radiance contains corresponding terms to those in the equation for the upwelling radiance except for the ones that are determined by the boundary conditions. Therefore the two terms which contain the reflection function do not occur. Instead in term 7 the direct solar radiation is introduced which is attenuated between the top of the atmosphere and the level τ_λ.

The radiative transfer equation in integral form also has no analytic solution because it is still an integral equation. There are several methods that give the numerical solution which are not treated here.

Since the RTE requires that the optical effects can in fact be expressed by the optical depth (see section 1.8.2), the transmission functions must be expanded as e-series no matter how small the wavelength intervals are, then the RTE must be solved separately for each term in the e-series and finally the results must be weighted and added.

1.9. The Radiative Transfer Equation as the Basic Equation for Remote Sensing

The radiative transfer equation has been presented so explicitly for two reasons: firstly, to show how all the interactions between radiation and matter can be given a joint quantitative description so that the total radiative transfer in the atmosphere can be described by just one equation.

Consequently, it must be possible to derive all the equations describing the radiation transport which are used in remote sensing applications from the RTE by adapting it to the particular problem.

This enables us to put the different remote sensing techniques into a wider context and is the second reason for having presented the RTE so explicitly.

3. Atmospheric Correction of Satellite Data

3.1. General

The aim is to conclude from the radiance measured on top of the atmosphere to the radiance leaving the surface. The problem is the intervening atmosphere which weakens the surface leaving radiance by extinction and reinforces it by scattering. In principle the aim is reached by solving the RTE. To do so, besides geometric properties the following quantities must be known: The surface reflection function, the optical depth of the atmosphere, the scattering phase function of the aerosol particles, and the absorption properties of minor atmospheric constituents like ozone and water vapor. The latter can mostly be parameterized by mean values, so we forget them for the moment.

The surface reflection function γ describes the amount of radiation which comes from one direction and is reflected to another direction, for all possible combinations of directions of incidence and reflection. The two extremes are

a) the isotropic reflection function which assumes an equal angular distribution of the reflected radiance independent from the direction of incidence, its maximum numerical value is $1/\pi$ for a perfect white Lambert diffuser, and
b) the perfect mirror reflection function described by the Fresnel formulas.

Natural surfaces are different from both extremes. Solid surfaces tend more to behave like the isotropic case, however their angular anisotropies vary inbetween one order of magnitude. Water surfaces behave more like the Fresnel mirror but differ considerably from it due to waves and white caps.

To date the reflection function of solid surfaces is known only in very limited cases, e.g. savannah, coniferous forest, pasture land (Figures 3.1.1 - 3.1.4). Only approximate or mean values are available for most solid surfaces. For water surfaces a good working approach is available [Cox/Munk] which accounts for waves depending on wind speed (Figure 3.1.5).

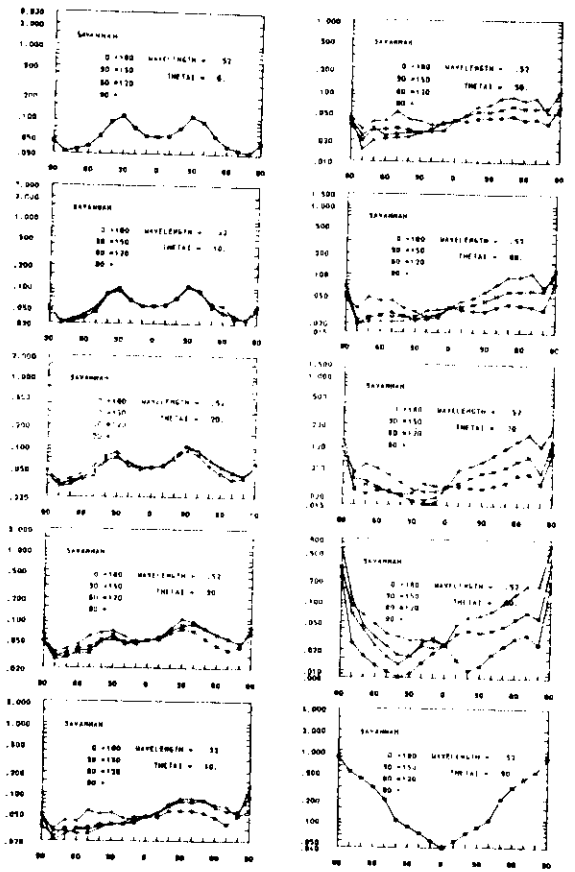

Fig. 3.1.1 Reflection functions of vegetated surfaces at 0.52 µm in dependence of zenith angle θ_r, azimuth ϕ_r and zenith angle of incidence θ_i: Savannah.

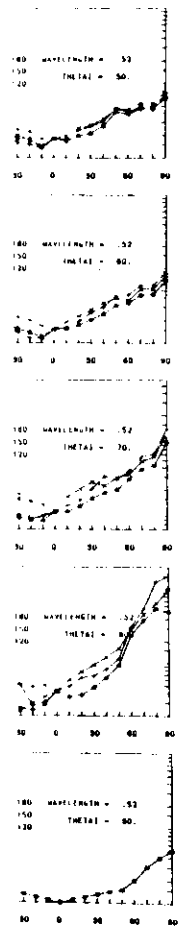

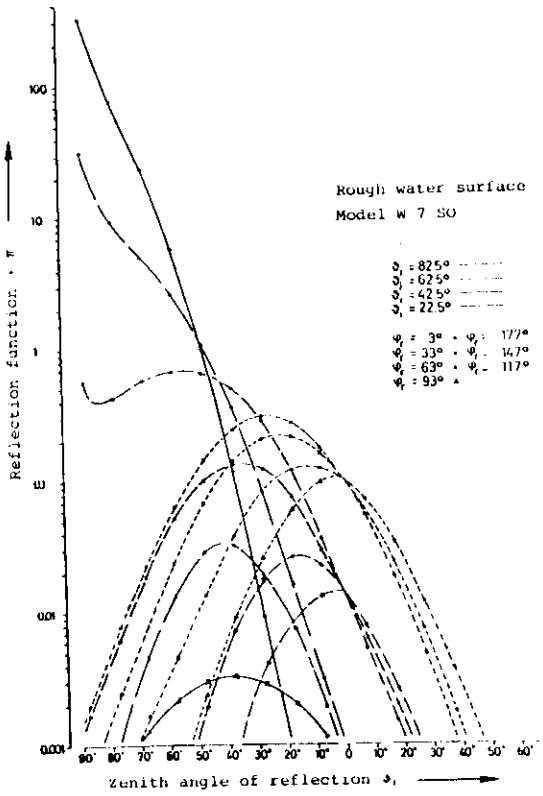

Fig. 3.1.5 Reflection function of water in dependence of zenith angle ϑ_r, azimuth φ_r and zenith angle of incidence ϑ_i.

.1: log.

67

The optical depth of the atmosphere T is highly variable in space and time and is usually not known. It can be measured either by ground based measurements, e.g. with actinometric measurements, or by measurement of the visual (meteorological) range, or from spaceborne instruments to a limited accuracy, as is shown in the next chapter. Over water surfaces some techniques have been developed which rely on the fact that water is nearly black in the infrared and then try to transfer infrared measurements to shorter wavelengths by assuming or knowing only the relative spectral behaviour of the optical depth [Gordon, Viollier, Deschamps, ISPRA- Report]. Over solid surfaces so far only active methods, using,- e.g., a laser as an artificial source, are expected to give good results. This is shown in more detail in the next chapter.

The scattering phase function p depends on the refractive index and on the aerosol size distribution. If the latter are known, p can be calculated according to the theory of Mie assuming spherical particles. However, the remote sensing of the refractive index and of the aerosol size distribution is very complicated and not yet achieved. Therefore usually the aerosol is classified into some typical cases and the scattering phase functions derived from those typical cases are used (Figure 3.1.6). One advantage is the rather weak dependence of the scattering functions on wavelength. This is used in the technique shown later in this chapter.

The conclusion of this discussion is that the solution of the RTE is generally not possible because

a) over solid surfaces neither γ nor T are known, and
b) over water surfaces neither T nor the ocean leaving radiance (under light) which is not included in the Fresnel formulas are known.

Therefore only approximative solutions are possible and with this we will deal now.

The approximation most commonly in use is the assumption of only single scattering. All higher orders of scattering are neglected. Herewith the RTE becomes analytically solvable and, hence, the necessary computer time is drastically reduced. But it should be kept in mind that the error introduced by this approximation can only be checked by means of the solution of the complete RTE including multiple scattering, at least for some

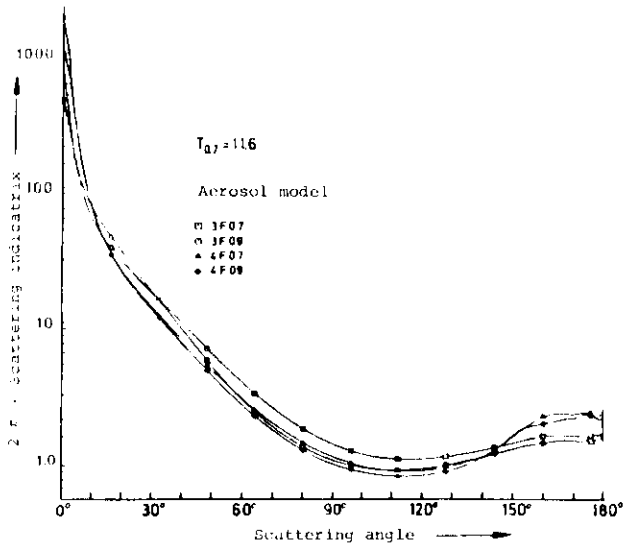

Fig. 3.1.6 Normalized phase functions for different size distributions.

typical cases covering the expected range of atmospheric variables.

The single scattering approximation also needs γ and T. Therefore the next step is to use a priori information on γ or T. But usually γ is the wanted quantity and therefore one must get some information on T. Knowledge of T must be available for all wavelengths of interest due to the unknown spectral behaviour of T which depends on refractive index and aerosol size distribution. However, keeping in mind the parameterization of the phase function based on an a priori classification of the aerosol type and, hence, of its refractive index and size distribution, on can derive appropriate information of the spectral dependence of the optical depth T. But at least at one wavelength the optical depth must be known. Over water this can be achieved at wavelengths beyond o.65 μm where water is essentially black, i.e. γ = 0. Herefore I will present an appro[illegible]e algorithm later in this chapter. Over land this can only be done by means of a ground based measurement of T near the site of interest because T varies not only in time but also in space. Measurements over a specific target area with known γ are usually not available near the site of interest.

A somewhat different technique is the measurement of the radiance difference of two adjacent surfaces. Given their inherent radiance difference

$$\Delta L_\lambda(T_\lambda,\mu,\varphi) = \Delta\gamma_\lambda(\mu_o,\mu;\varphi-\varphi_o)\ E_\lambda^o\ \mu_o\ e^{-T_\lambda/\mu_o}$$

$$+ \int_o^{2\pi}\int_o^1 \Delta\gamma_\lambda(\mu,\mu';\varphi-\varphi')\ L_\lambda(T_\lambda,-\mu',\varphi')\mu'd\mu'd\varphi'$$

the measured reduced radiance difference on top of the atmosphere is

$$\Delta L_\lambda(0,\mu,\varphi) = \Delta\gamma_\lambda(\mu_o,\mu;\varphi-\varphi_o)\ E_\lambda^o\ \mu_o\ e^{-T_\lambda/\mu_o}\ e^{-T_\lambda/\mu}$$

$$+ \int_o^{2\pi}\int_o^1 \Delta\gamma_\lambda(\mu,\mu';\varphi-\varphi')\ L_\lambda(T_\lambda,-\mu',\varphi')\mu'd\mu'd\varphi'\ e^{-T_\lambda/\mu}$$

This holds if the phase function of the areosol is assumed to be the same over both surfaces which is most likely near the border of the two adjacent sufaces.

Dividing the measured radiance differences by the inherent radiance difference yields

$$\frac{\Delta L_\lambda(0,\mu,\varphi)}{\Delta L_\lambda(T_\lambda,\mu,\varphi)} = e^{-T_\lambda/\mu}$$

and hence,

$$T_\lambda = \mu \ln \frac{\Delta L_\lambda(T_\lambda,\mu,\varphi)}{\Delta L_\lambda(0,\mu,\varphi)}$$

This formula includes all multiple scattering except that caused by the different surface reflection function.

The inherent radiance difference can be measured with airborne instruments. But it should be noticed that the radiance difference itself is dependent on the solar elevation angle and on T. So such airborne measurements must be made at the same time as are the satellite measurements.

So far we have seen that the main problem in atmospheric correction of satellite data is how to get sufficient information on the optical depth of the atmosphere. However, all proposed methods are based on the assumption, that the measured radiances on top of the atmosphere are absolutely calibrated in radiance units. This follows from the RTE which describes the measured radiance essentially as the sum of two terms:

$$L_\lambda(0,\mu,\varphi) = L_\lambda(T_\lambda,\mu,\varphi)\, e^{-T_\lambda/\mu} + L_{P\lambda}$$

$L_{P\lambda}$ stands for path radiance and includes all photons into the direction (μ,φ) which are not reflected by the surface into the direction (μ,φ). The path radiance must be substracted from the measured radiance to proceed to the quantities of interest and both must therefore be known absolutely.

3.2. Landsat

Due to its broad spectral bands quantitative measurements are made mostly over land surfaces. Because the MSS is not absolutely calibrated, use can be made from known calibration targets like White Sands, provided simul-

3. AVHRR

Table 2-1. Spectral characteristics of the TIROS-N/NOAA AVHRR instruments

Four-channel AVHRR, TIROS-N				
Ch 1 0.55-0.9 μm	Ch 2 0.725-1.1 μm	Ch 3 3.55-3.93 μm	Ch 4 10.5-11.5 μm	Ch 5 Data from Ch 4 repeated
Four-channel AVHRR - NOAA-A, -B, -6 and -8				
Ch 1 0.58-0.68 μm	Ch 2 0.725-1.1 μm	Ch 3 3.55-3.93 μm	Ch 4 10.5-11.5 μm	Ch 5 Data from Ch 4 repeated
Five-channel AVHRR, NOAA-D, -F, -G, -H, -I and -J				
Ch 1 0.58-0.68 μm	Ch 2 0.725-1.1 μm	Ch 3 3.55-3.93 μm	Ch 4 10.3-11.3 μm	Ch 5 11.5-12.5 μm

Note Changes to the above deployment scheme may occur as a result of instrument availability or changing requirements.

Table 2-2. AVHRR instrument parameters

Parameter	Value
Calibration	Stable blackbody and space for IR channels. No inflight visible channel calibration other than space.
Cross track scan	±55.4° from nadir
Line rate	360 lines per minute
Optical field of view	1.3 milliradians
Ground resolution (IFOV)(1)	1.1 km @ nadir
Infrared channel NEΔT(2)	<0.12 K at 300 K
Visible channel S/N(3)	3 1 @ 0.5% albedo

1) Instantaneous field of view
2) NEΔT - Noise equivalent differential temperature
3) Signal-to-noise ratio

2.2.1 High Resolution Infrared Radiation Sounder (HIRS/2)

The HIRS/2 is an adaptation of the HIRS/1 instrument flown on the Nimbus-6 satellite. The instrument, built by the Aerospace/Optical Division of the International Telephone and Telegraph Corporation, Fort Wayne, Indiana, measures incident radiation in 19 regions of the IR spectrum and one region of the visible spectrum.

Table 2-3 is a listing of the nominal HIRS/2 parameters.

TIROS-N/NOAA A-G Summary Sheet

Spacecraft	:	Total weight (includes expendables)	1421 Kg (3127 lbs)
Payload	:	Weight including tape recorders	194 Kg (427 lbs)
	:	Reserved for growth	36.4 Kg (80 lbs)

Instrument Complement:

Advanced Very High Resolution Radiometer (AVHRR)
High Resolution Infrared Radiation Sounder (HIRS/2)
Stratospheric Sounder Unit (SSU)
Microwave Sounder Unit (MSU)
Data Collection System-ARGOS (DCS)
Space Environment Monitor (SEM)

Spacecraft Size: 3.71 meters in length (146 inches)
1.88 meters in diameter (74 inches)

Solar Array : 2.37 m X 4.91 m : 11.6 square meters
(7.8 ft X 16.1 ft : 125 sq ft)

420 watts, end of life, at worst solar angle

Power Requirement: Full operation-330 watts
Reserved for growth-90 watts

Attitude Control System: 0.2° all axes
0.14° determination

Communications

Command Link	:	148.56 MHz
Beacon	:	136.77; 137.77 MHz
S-Band	:	1698; 1702.5; 1707 MHz
APT	:	137.50; 137.62 MHz
DCS (uplink)	:	401.65 MHz
Data Processing	:	All digital (APT; analog)
Orbit	:	833; 870 km nominal
Launch Vehicle	:	Atlas E/F
Lifetime	:	2 years planned

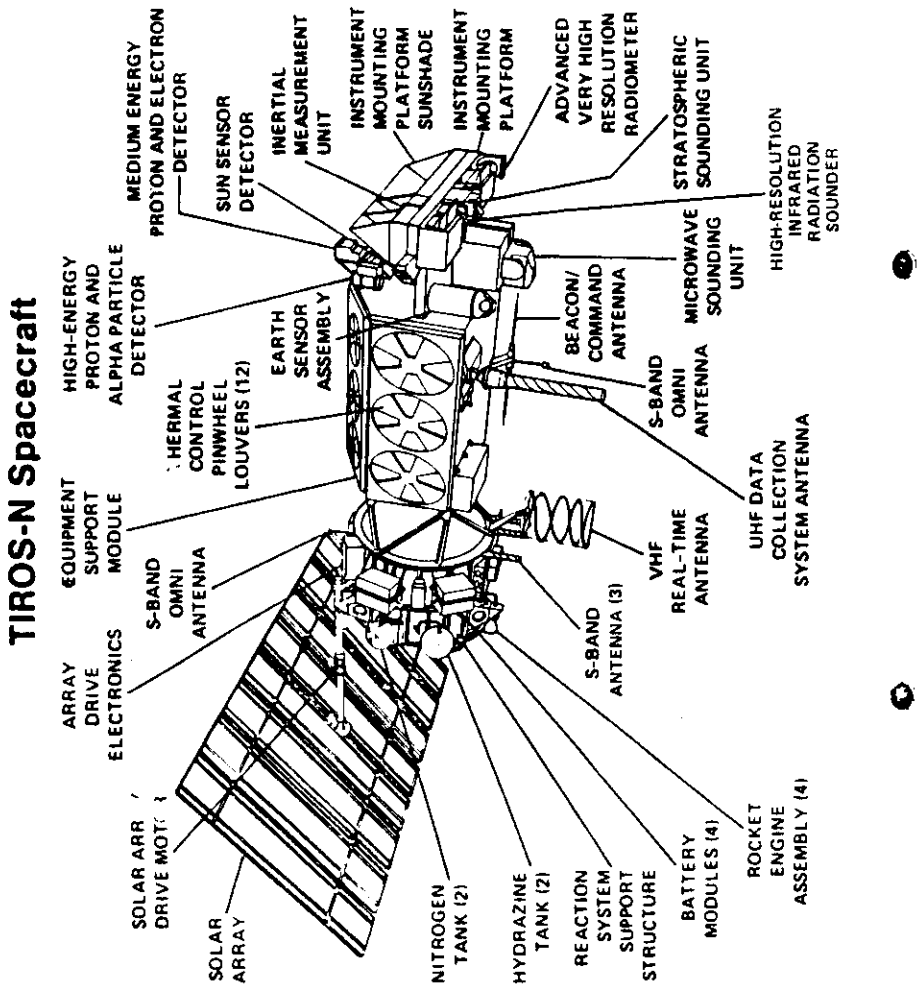

FUTURE U.S. POLAR-ORBITING METEOROLOGICAL SATELLITES

Advanced Systems Concepts Group
Systems Planning and Development Staff

1. INTRODUCTION

Since the launch of the first meteorological satellite, TIROS I, on April 1, 1960, the U.S. has maintained in orbit an array of spacecraft in support of weather forecasting, and for monitoring of natural environmental hazards. Following the first TIROS (Television and Infrared Operational Satellite), the National Aeronautics and Space Administration supported the development of a series of "NIMBUS" experimental remote sensing spacecraft for weather observations, which served as test vehicles for ever-more-advanced sensors. As spacecraft advances and ground station processing reached a stage permitting quantitative analysis of remote sensing data, research satellites gave way to operational, "NOAA-series" platforms.

The current generation of U.S. polar meteorological satellites began with the launch of NOAA-7 (C) in 1981. (NOAA-series spacecraft have letter designations before launch, and are then numbered when operational in orbit.) The same family of platforms will continue through NOAA-J, slated for launch in March 1989. In a procurement of three more spacecraft, NOAA-K, -L, -M, small changes in the space platform are planned to support several significant changes in instrumentation. After NOAA-K, -L, -M (1990-92), a thorough redesign of the space platform is projected, accompanied by an increase in the number of sensors carried, to include modified versions of the present sensors, and also experimental sensors envisioned as replacements for the present operational sensors.

2. CURRENT NOAA-SERIES SPACECRAFT (NOAA-C THROUGH -J)

The present NOAA-Series polar orbiting spacecraft (See Table I) weighs more than 1000 Kg and carries an array of about eight sensors and data-relay systems, of which the most important are a high resolution surface imager (AVHRR), and an ensemble of three instruments lumped together as the TOVS (TIROS Operational Vertical Sounder). These instruments (HIRS, SSU, and MSU) provide sounding data, that is, values of emitted infrared and microwave brightness values from the Earth's surface and atmosphere, from which profiles of the atmospheric temperature, and moisture content aloft, may be calculated. While the calculation of soundings formerly required a major meteorological processing center, this can now be carried out by a tabletop computer. Soundings form the major satellite input to worldwide numerical weather prediction. Soundings are supplemented in prediction models by surface temperature values derived from AVHRR brightness values. (Winds calculated from apparent cloud motion as seen in sequential geostationary satellite images, are also of great value.)

Three of the four instruments providing imagery and soundings from the NOAA-series platform (AVHRR, HIRS, and SSU) operate in the infrared portion of the spectrum. (MSU is a four-channel Microwave Sounder Unit.) Since clouds are opaque to the passage of infrared energy, neither surface temperatures nor soundings are possible through cloud cover using infrared instruments. In winter, when much of the continental United States is cloud decked, this causes a serious data loss. While course soundings can be calculated from MSU data, the MSU's four channels (between 50 and 57 GHz) do not describe a detailed profile of temperature or moisture versus height.

3. NOAA-K, -L, -M

The major change planned for NOAA-K and subsequent satellites is the installation of an Advanced Microwave Sounding Unit (AMSU), a 20-channel sounder operating in frequencies between 23 and 183 GHz, including the 50 GHz channels used in the MSU. HIRS is retained; MSU and SSU are dropped. The resulting increase in sounding data is expected to reduce the error in soundings calculated from satellite data by about one-half. Other products to be calculated from AMSU microwave data include water vapor profiles, precipitation and global sea ice coverage.

AVHRR will have changes made in several of its channels (see Table II). Channels 1 and 2 will be modified to make the visible and near-IR data more useful for the calculation of a "vegetation index," a data product indicating the "greenness" of the region imaged. Channel 3 will be replaced by a switched channel, for sunlit and dark scenes. Channel 3A remains unchanged in spectral content. Channel 3B will enhance determination of cloud cover, versus surface snow and ice cover. For Channels 1 and 2, slight changes are proposed in the on-board processing algorithm, to enhance the resolution of brightness in the low-albedo region of the instrument's brightness curve. The change is not expected to be detectable by direct data readout users.

The HIRS Channel 20 is to be broadened, to enhance its value as a data source for studies of the Earth radiation budget. The change seeks to compensate researchers for the loss of the experimental Earth Radiation Budget Experiment (ERBE) instrument. At present, the HIRS Channel 20 covers only 0.6 to 0.7 um. Replacement of a visible radiation (silicon) detector by a thermal radiation (germanium) detector in the channel will widen the spectral response from 0.2 to approximately 2 um, without the necessity of an optical system redesign.

An orbital change is scheduled for NOAA-H and subsequent spacecraft. The time for equatorial crossings is to be advanced from 1430 to 1330 local times. A sun-synchronous orbit is retained. The planned change required a thorough redesign of the spacecraft's thermal controls and instrument shades, since the spacecraft will observe the sun constantly at higher viewing angles, during all sunlit flight times. The change is planned to coordinate Eastern Pacific data collection with a change scheduled by the U.S. National Weather Service, to move forward the start-up time of its numerical prediction runs.

Installation of an Ocean Color Instrument (OCI), similar to the earlier Coastal Zone Color Scanner (CZCS), is also under consideration for the NOAA-K, -L, -M purchase. Flight of the OCI would increase data collection in support of near-shore marine interests including fisheries, and environmental monitoring of rivers, estuaries, and continental-shelf oceans.

Whether or not an Ocean Color Instrument is added to NOAA-K, -L, -M, the addition of the AMSU will force a change in the telemetry bands used by the spacecraft for direct to user broadcasts and data dumps to ground stations. Additional bandwidth is not available at the S-Band frequencies now used. In addition, one the beacon frequencies now used (136.77 MHz), falls into a band slated to be reallocated to use by commercial aviation, beginning in 1990. Various scenarios are now under consideration, in an effort to achieve sufficient data flows with a minimum impact on spacecraft and ground station telemetry hardware, and also so minimize the cost-impact on direct broadcast data users worldwide.

Tables III and IV show payloads scheduled for NOAA-C through -M, and details of NOAA-K, -L, -M changes.

4. FUTURE NOAA-SERIES SATELLITE SYSTEMS

With NOAA-K, -L, -M close to determined, extensive satellite improvements are now possible only aboard spacecraft to be purchased for launch in the decade of the 1990s and beyond.

Proposals are now under consideration within NOAA for a "block change", that is, for development of a new satellite bus, to replace the existing platform in the early 1990s. The major purpose of this change is to permit flight of experimental sensors, along with a required complement of operational imagers and sounders. Candidates for development and experimental flight include active microwave instruments for measurement of winds and ocean surface parameters. (Active instruments send out pulses of microwave energy, comparable to radar units.) Two instruments, an active Synthetic Aperture Radar, and a multi-spectral Ocean Color Instrument (if not already operational), could provide data for marine interests including sub-surface contours in near-continent waters. An active Altimeter could determine ocean surface heights to accuracies sufficient to permit monitoring of the strengths and directions of ocean currents. A major element of a new bus would be an enlarged solar-cell power supply, to permit operation of a larger suite of instruments. Also under consideration are plans for modular construction of the spacecraft, to facilitate shuttle repair or replacement of components.

TABLE I

"ADVANCED TIROS-N" (NOAA-C through -J) SUMMARY SHEET

Spacecraft: Total Weight - 1,009 Kg (2,200 lbs)
(Excludes expendables)

Payload: Weight, including tape recorders - 386 Kg (850 lbs)

Instrument Complement: Advanced Very High Resolution Radiometer (AVHRR/2)
High Resolution Infrared Radiation Sounder (HIRS/2)
Stratospheric Sounder Unit (SSU)
Microwave Sounder Unit (MSU)
ARGOS Data Collection System (DCS)
Space Environment Monitor (SEM)
Search and Rescue (SAR) Satellite Aided Tracking (SARSAT)
Solar Backscatter Ultra Violet Radiometer (SBUV/2) - NOAA F and on -
Earth Radiation Budget Experiment (ERBE) - NOAA F and G only

Spacecraft Size: 3.71 meters in length (165 inches)
1.88 meters in diameter (74 inches)

Solar Array: 2.37 m x 4.91 m: 11.6 square meters
(7.8 ft x 16.1 ft: 125 square feet)

515 watts, end of life at worst solar angle
(high efficiency solar cells)

Power Requirement: Full operation - 475 watts
Reserved - 40 watts

Attitude Control System: 0.2° all axes
0.14° determination

Communications: Command Link - 148.56 MHz
Beacon - 136.77; 137.77 MHz
S-Band - 1698; 1702.5; 1707 MHz
APT - 137.50; 137.62 MHz
DCS (uplink) - 401.65 MHz
SAR - 1544.5 MHz
SAR (uplink) - 121.5; 243.0; 406 MHz

Data Processing: All digital (APT translated to Analog)

Orbit: 833; 870 Km nominal, sun synchronous

TABLE II

POLAR IMAGERS AND SOUNDERS (NOAA-C through -J)

Sensors and Functions

o Advanced Very High Resolution Radiometer (AVHRR/2)
1.1 km resolution; <2600 km swath width

Channels	Wavelengths (um)	Primary Uses
1	0.58- 0.68	Daytime cloud/surface mapping
2	0.725-1.10	Surface water delineation, ice and snow melt
3	3.55 -3.93	Sea surface temperature, nighttime cloud mapping
4	10.30-11.30	Sea surface temperature, day and night cloud mapping
5	11.50-12.50	Sea surface temperature, day and night cloud mapping

o TIROS Operational Vertical Sounder (TOVS)

(A three-sensor atmospheric sounding system)

(1) High Resolution Infrared Radiation Sounder (HIRS/2)
17.4 km resolution

Channels	Wavelengths (um)	Primary Uses
1-5	14.95-13.97	Temperature profiles, clouds
6-7	13.64-13.35	Carbon dioxide and water vapor bands
8	11.11	Surface temperature, clouds
9	9.71	Total O_3 concentration
10-12	8.16- 6.72	Humidity profiles, detection of thin cirrus clouds
13-17	4.57- 4.24	Temperature profiles
18-20	4.00- 0.69	Clouds, surface temperatures under partly cloudly skies

TABLE II (CON'T)

POLAR IMAGERS AND SOUNDERS (NOAA-C through -J)

(2) Stratospheric Sounding Unit (SSU)
147.3 km resolution

Channels	Wavelengths (um)	Primary Uses
1-3	approx. 15	Temperature profiles

(3) Microwave Sounding Unit (MSU)
105 km resolution

Channels	Frequencies	Primary Uses
1	50.31 GHz	
2	53.73 GHz	Temperature soundings through clouds
3	54.96 GHz	
4	57.95 GHz	

SPACECRAFT	C(7)	D	E(8)	F	G	H	I	J	K	L	M
AM/PM	(PM)	AM	(AM)	PM	AM	PM	PM	AM	PM	AM	PM
SCHED. LAUNCH	(6/81)	8/87	(3/83)	10/84	8/85	10/86	10/88	8/89	10/90	8/91	10/92
FAILED DATE			7/84								
INSTRUMENT											
AVHRR	YES	YES	YES	YES	YES/1	YES	YES	YES	YES/2	YES/2	YES/2
HIRS/2	YES	YES	YES	YES	YES	YES/1	YES/1	YES/1	YES/2	YES/2	YES/2
AMSU	NO	NO	NO	NO	NO	NO	NO	NO	YES	YES	YES
SSU	YES	DUMMY	YES	YES	DUMMY	YES	YES	DUMMY	NO	NO	NO
MSU	YES	YES	YES	YES	YES	YES	YES	YES	NO	NO	NO
DCS (ARGOS)	YES	YES	YES	YES	YES	YES	YES	YES	YES/1	YES/1	YES/1
SAR	NO	NO	YES	YES	YES	YES	YES	YES	YES	YES	YES
SBUV/2	NO	NO	BALLAST	YES	NO	YES	YES	NO	YES	NO	YES
ERBE SCANNER	NO	NO	BALLAST	YES	YES	DUMMY	DUMMY	DUMMY	NO	NO	NO
ERBE NON-SCANNER	NO	NO	BALLAST	YES	YES	DUMMY	DUMMY	DUMMY	NO	NO	NO
SEM TED	YES	DUMMY	YES	DUMMY	YES	DUMMY	YES	DUMMY	YES	YES	YES
MEPED	YES	DUMMY	YES	DUMMY	YES	DUMMY	YES	DUMMY	YES	YES	YES
MEPAD	YES	DUMMY	NO	NO	NO	NO	NO	NO	NO	NO	NO

NOTE: Ballast denotes addition to balance spacecraft center of gravity. Dummy denotes a physical simulation model with proper weight, thermal characteristics and appropriate electrical terminations.

AVHRR - /1 denotes 4 channel instrument; /2 denotes 5.5-channel (one switched channel) instrument, with changed channel gains.

HIRS/2 - /1 indicates instrument HIRS/2I, /2 shows HIRS/2II. (See text.)

DCS - /1 indicates a doubling of system capacity.

SBUV/2 - SBUV instrument is carried only on p.m. flights.

MEPAD - MEPAD has been shifted to the GOES spacecraft.

TABLE IV

COMPARISON OF SENSORS AND SYSTEMS FOR NOAA-SERIES, POLAR-ORBITING SATELLITES

FUNCTION	NOAA-E through -J	NOAA-K through -M
IMAGING		
NUMBER OF CHANNELS (AVHRR)	5	6
SPATIAL RESOLUTION		
VISIBLE	0.5 KM	SAME
IR	1.0 KM	SAME
SPECTRAL SPECIFICATIONS	CH 1: 0.58-0.68 um	CH 1: SAME
	CH 2: 0.7 -1.1 um	CH 2: 0.82-0.87 um
	CH 3: 3.55-3.93 um	CH 3a: 1.57-1.78 um*
		CH 3b: 3.55-3.93 um*
	CH 4: 10.3-11.3 um	CH 4: SAME
	CH 5: 11.5-12.4 um	CH 5: SAME
	* CHANNELS 3a and 3b ARE TIME SHARED	
SOUNDING		
NUMBER OF CHANNELS		
IR (HIRS/2)	23	20
MICROWAVE (MSU, AMSU)	4	20
SPATIAL RESOLUTION		
IR (HIRS)	17.5 KM (NADIR)	SAME
MICROWAVE (TEMPERATURE)	110.0 KM (NADIR)	40.0 KM (NADIR)
MICROWAVE (WATER VAPOR)	N/A	15.0 KM (NADIR)
MICROWAVE (ICE)	N/A	15.0 KM (NADIR)
SPACE ENVIRONMENT MONITOR	INCLUDED	NO CHANGE
OZONE	SBUV (PM ONLY)	SBUV (PM ONLY)
DATA COLLECTION SYSTEM	INCLUDED	INCREASED CAPACITY
SEARCH AND RESCUE	INCLUDED	NO CHANGE
EQUATOR CROSSING TIMES		
TWO SATELLITE SYSTEM	AM 07:30 LOCAL	AM NO CHANGE
	PM 14:30 LOCAL	PM 13:30 LOCAL*
	* CHANGE BEGINS ON NOAA-H	
COMMUNICATIONS		
AUTOMATIC PICTURE TRANSMISSION (APT)	137.50 MHz 137.62 MHz	NO CHANGE NO CHANGE
DIRECT SOUNDING BROADCAST	136.77 MHz 137.77 MHz	S-BAND AT APPROX. 1609.5 MHz
HIGH RESOLUTION PICTURE TRANSMISSION (HRPT)	1698.0 MHz 1702.5 MHz 1707.0 MHz	NO CHANGE

METEOSAT SECOND GENERATION

VIRI : 8 SPECTRAL CHANNELS

NOAA AVHRR/2 : 5 SPECTRAL CHANNELS

MSG/VIRI	AVHRR/2	Channel
0.60 - 0.67 µm	0.58 - 0.68 µm	1
0.74 - 0.89 µm	0.72 - 1.10 µm	2
1.53 - 1.70 µm		
3.5 - 3.9 µm	3.55 - 3.93 µm	3
5.8 - 6.7 µm		
6.9 - 7.3 µm		
10.3 - 11.3 µm	10.3 - 11.3 µm	4
11.5 - 12.5 µm	11.5 - 12.5 µm	5

COMMON FEATURES :

- SPLIT WINDOW VIS
- SPLIT WINDOW IR
- CLOUD/SNOW/ICE CHANNEL

ADVANCED MEDIUM RESOLUTION IMAGING RADIOMETER (AMRIR)

James C. Fischer
Advanced Systems Division
National Environmental Satellite, Data and Information Service

The AMRIR has been specified and designed to replace and improve the Advance Very High Resolution Radiometer (AVHRR) and the High resolution Infrared Radiometer Sounder (HIRS). The AMRIR contains the six spectral channels that were contained in the AVHRR, NOAA K, L, M version, AVHRR/3, with some minor adjustments to the spectral bands. In addition to the six AVHRR channels that are contained in the AMRIR, there have been added three sounding channels, a total ozone channel and an additional sea surface temperature channel. Simulation of sounding data has shown that this combination of channels, when combined with the twenty AMSU channels, offer a sounding accuracy that is comparable to the HIRS/AMSU combination on NOAA K, L, M series.

The spectral characteristics of the AMRIR are as follows:

CHANNEL	CENTER FREQUENCY	50% RESPONSE BW	S/N
1	665.0 ±2.0 nm	655.0 ±1.0 nm 675.0 ±1.0 nm	10:1
2	855.0 ±2.0 nm	840.0 ±2.0 nm 870.0 ±2.0 nm	10:1
3	1.61 ±0.01 micron	1.58 ±0.01 micron 1.64 ±0.01 micron	20:1
4	1030 ±4.0 cm^{-1}	Total 50% BW 25 cm^{-1}	0.2°K
5	2210 ±4.4 cm^{-1}	Total 50% BW 15 cm^{-1}	0.2°K
6	2250 ±4.4 cm^{-1}	Total 50% BW 15 cm^{-1}	0.2°K
7	735.5 ±1.8 cm^{-1}	Total 50% BW 9 cm^{-1}	0.2°K
8	3.72 ±0.06 micron	3.63 ±0.06 micron 3.83 ±0.06 micron	0.1°K
9	4.01 ±0.06 micron	3.92 ±0.06 micron 4.10 ±0.06 micron	0.1°K
10	10.8 ±0.06 micron	10.30 ±0.06 micron 11.30 ±0.06 micron	0.1°K
11	12.0 ±0.06 micron	11.50 ±0.06 micron 12.50 ±0.06 micron	0.1°K

The instantaneous field-of-view (IFOV) at nadir for channels 1, 2, 3, 8, 9, 10 and 11 is 800 meters. The signal-to-noise specified for these channels is for the 800 meter IFOV. The IFOV for channels 4 through 7 is specified at 3.75 km. The 3.75 km IFOV for channels 4 through 7 is derived from the requirement that the AMRIR IFOV be one fourth the IFOV of the AMSU-B. The signal-to-noise for channels 4 through 7 is based on a 3.75 km IFOV.

The selection of the spectral bands, IFOV and signa.-to-noise was based on the following requirements for the various channels:

Channel 1 - Products derived from this channel include visible imaging products such as clouds, snow, ice, vegetation, hydrology, water and floods. Quantitative products include Earth radiation budget and aerosols. This channel is a replacement for the AVHRR channel 1 with the spectral bandwidth being narrower to provide better information on aerosols.

Channel 2 - Products derived from this channel include visible imaging products such as clouds, snow, ice, vegetation, hydrology, water and floods. Quantitative products, include Earth radiation budget and aerosols. This channel is a replacement for the AVHRR channel 2 with the spectral bandwidth being narrower to provide better information on aerosols and to avoid water vapor contamination from the water vapor line at 890 nm.

Channel 3 - Purpose of this channel is for snow/cloud discrimination. Channel is identical to channel 3A on the AVHRR/3.

Channel 4 - Total Ozone monitoring channel. Carryover from the HIRS and is equivalent to channel 9 of the HIRS. Provides ozone information in the infrared region that is not available from SBUV data.

Channel 5 - Atmospheric sounding channel. Equivalent HIRS channel is 14. This channel is used in conjunction with channels 4, 6, 7 and the window channels 8, 9, 10 and 11 to provide atmospheric soundings.

Channel 6 - Atmospheric sounding channel. Equivalent HIRS channel is 15. This channel is used in conjunction with channels 4, 5, 7 and the window channels 8, 9, 10 and 11 to provide atmospheric soundings.

Channel 7 - Atmospheric sounding channel. No equivalent HIRS channel. This channel was selected to provide maximum information and high accuracy with minimum spectral regions for atmospheric sounding. This channel is used in conjunction with channels 4, 5, 6 and the window channels 8, 9, 10 and 11 to provide a sounding

product which is of higher accuracy than the HIRS/MSU combination on pre-NOAA K era satellites. The combination of AMRIR/AMSU provides temperature soundings comparable to that of HIRS/AMSU combination.

Channel 8 - Window channel used for measuring sea surface temperature and temperature sounding. This channel, used in conjunction with channel 9, will provide a sea surface temperature accuracy of 0.5°K. Equivalent channel on AVHRR/3 was 3B.

Channel 9 - Window channel used for measuring sea surface temperature and temperature sounding. This is a new channel and there is not an equivalent channel on the AVHRR/3. This channel was added to provide an improvement to the accuracy of sea surface temperature from the AVHRR/3 of 0.75°K to a estimated accuracy of 0.5°K.

Channel 10 - Window channel used for infrared imaging, sea surface temperature, temperature sounding and nighttime clouds. Equivalent channel on the AVHRR/3 was channel 4.

Channel 11 - Window channel used for infrared imaging, sea surface temperature, temperature sounding and nighttime clouds. Equivalent channel on the AVHRR/3 was channel 5.

The AMRIR has been specified to improve the overall capability of the AVHRR and the HIRS. Some of the major additional benefits of the AMRIR are as follow:

-- Increased imaging spatial resolution from 1100 meters to 800 meters.

-- Increased radiometric sensitivity, AMRIR will have a 12-bit digital resolution versus 10-bit for the AVHRR.

-- Increased sounding spatial resolution from 21 kilometers for the HIRS to 3.75 kilometers for the AMRIR.

-- Improved thermal calibration.

-- Visible calibration will be available in the AMRIR whereas the AVHRR had no visible calibration.

-- Absolute coalignment of imaging and sounding channels.

-- Increased sensitivity in the window channels for 0.1°K in the AMRIR versus 0.25°K in the AVHRR.

-- Increased geographic coverage for soundings, AMRIR scans out to 56° from nadir versus 49° for HIRS.

-- Specifically being designed for co-registration with the AMSU-B fields-of-view.

The AMRIR is anticipated to begin phase C/D activities in 1990 with the first flight scheduled for 1997.

BENEFITS OF AMRIR VS. AVHRR/HIRS

4. APOLLO

SYSTEM

o DESIGNED FOR FOUR YEAR LIFETIME VS. 2 YEARS FOR AVHRR/HIRS

o SPECIFICALLY DESIGNED FOR FLIGHT ON NEXT GENERATION SPACECRAFT RATHER THAN HAVING TO ADOPT 20 YEAR OLD TECHNOLOGIES

IMAGING

o INCREASED SPATIAL RESOLUTION FROM 1100 METERS TO 800 METERS

o VISIBLE CHANNEL CALIBRATION FOR QUANTITATIVE APPLICATIONS

o UPGRADED BLACK BODIES FOR IMPROVED THERMAL CALIBRATION

o DEDICATED CHANNELS FOR FIRE DETECTION AND SNOW/CLOUD DESCRIMINATION

o AN ADDITIONAL CHANNEL FOR SST DETERMINATION (SPLIT WINDOW AT 3.8 MICRON)

o INCREASED RADIOMETRIC PRECISION FOROM 10 BIT TO 12 BIT (IMPROVES SENSITIVITY FOR AEROSOL, RADIATION BUDGET, AND SST DETERMINATIONS)

SOUNDING

o INCREASED SPATIAL RESOLUTION FROM 21.0 KM TO 3.75 KM (MORE CLOUD FREE RETRIEVALS)

o INCREASED WINDOW CHANNEL SENSITIVITY FROM 0.25 K TO 0.1 K

o INCREASED GEOGRAPHIC COVERAGE (FROM 49 DEG SCAN TO 56 DEG)

o ABSOLUTE COALIGNMENT WITH IMAGING CHANNELS

o DESIGNED FOR COREGISTRATION WITH AMSU-B FIELDS OF VIEW (PRECISELY ONE QUARTER AMSU-B FOV)

PROGRAMMATIC

o ALLOWS FOR RECOMPETITION OF IMAGER/IR SOUNDER RATHER THAN CONTINUING PRESENT SOLE SOURCE ARRANGEMENT

INT. J. REMOTE SENSING, 1988, VOL. 9, NO. 1, 123–150

An improved method for detecting clear sky and cloudy radiances from AVHRR data

R. W. SAUNDERS

Meteorological Office Unit, Hooke Institute for Atmospheric Research, Clarendon Laboratory, Oxford OX1 3PU, England

and K. T. KRIEBEL†

Institute for Atmospheric Physics, D.F.V.L.R. Oberpfaffenhofen, 8031 Wessling, F.R. Germany

(Received 16 February 1987, in final form 17 June 1987)

Abstract. To obtain accurate estimates of surface and cloud parameters from satellite radiance data a scheme has to be devised which identifies cloud-free and cloud-filled pixels (i.e. fields of view). Such a scheme has been developed for application to high resolution (1·1 km pixel) images recorded over Western Europe and the North Atlantic by the AVHRR on the TIROS-N/NOAA polar orbiters. The scheme consists of five daytime or five night-time tests applied to each individual pixel to determine whether that pixel is cloud-free, partly cloudy or cloud-filled. The pixel is only identified as cloud-free or cloud-filled if it passes all the tests to identify that condition; otherwise it is assumed to be partly cloudy. Surface parameters (e.g. skin temperature, reflectance, vegetation index, snow cover) can then be inferred from the cloud-free radiances, and cloud parameters (e.g. cloud top temperature, optical depth and liquid water content) from the cloud-filled radiances. Only fractional cloud cover is derived from the partly cloudy pixels which, together with the number of cloud-filled pixels, gives total cloud cover over a given area. The scheme has been successfully applied to data for all seasons, including images with unusually cold or warm surface temperatures. To assess the method both daytime and night-time NOAA-9 passes over the U.K. were obtained for a week in April 1985 and some results from this data set are presented here.

1. Introduction

Data from the Advanced Very High Resolution Radiometer (AVHRR) on board the TIROS-N/NOAA-n polar orbiter series of meteorological satellites are being increasingly used for deriving quantitative meteorological and surface variables. This is due to the ease with which the data can be obtained at a relatively low cost and to the horizontal resolution which can be as high as 1·1 km close to the sub-satellite track. In addition one satellite passes over the same area twice in 24 hours at mid-latitudes which leads to the possibility of four observations per day for a two-satellite system.

To make estimates of surface variables from upwelling radiances measured by an instrument such as the AVHRR, cloud-free fields of view (pixels) have to be identified. Variables such as sea surface temperature (SST) (Llewellyn-Jones *et al.* 1984, McClain *et al.* 1985), land surface temperature (Price 1984), surface reflectance (Pinker 1985) and vegetation index (McGinnis and Tarpley 1985) can all be inferred from cloud-free AVHRR pixels. Atmospheric variables are also measured by infrared sounders (e.g.

† This work was carried out during a one year visit to Oxford.

the High Resolution Infrared Radiation Sounder, HIRS, on the same satellite as the AVHRR). Clear sky radiances are normally required in order to obtain accurate temperature profiles (Eyre and Watts 1987). Conversely, to infer cloud properties from the radiances as outlined by Kriebel (1986), cloud-filled fields of view must be identified. To obtain cloud cover, the fractional cloudiness of all pixels which are neither cloud-free nor cloud-filled also has to be determined.

Interest has increased in recent years in deriving a global cloud climatology from satellite data, as cloud is one of the most important factors which influence climate. Hence there has been much work done in developing algorithms for detecting and classifying clouds in remotely-sensed data (e.g. Reynolds and Vonder Haar 1977, Coakley and Bretherton 1982, Phulpin *et al.* 1983, Minnis and Harrison 1984, Olesen and Grassl 1985, Arking and Childs 1985, Rossow *et al.* 1985, Saunders 1985, Chou *et al.* 1986, D'Entremont 1986). A comprehensive data set designed for the application of cloud algorithms has been collected by the International Satellite Cloud Climatology Project (ISCCP) (Schiffer and Rossow 1983) which has obtained data from both geostationary and polar orbiting satellites. However the majority of the algorithms developed are for cloud classification rather than cloud clearing and so the same algorithms cannot be used to detect surface parameters as well as cloud parameters. Once high resolution AVHRR data became available it was clear that to derive accurate surface and cloud parameters routinely, an automated scheme to detect cloud-free and cloud-filled pixels would have to be developed.

The basis of such a scheme to detect cloud-free pixels has already been outlined in a recent paper by Saunders (1986a) though a few additions and improvements have since been made. It is the intention of this paper to describe these and to introduce the methods used to detect cloud-filled pixels and to infer fractional cloudiness for individual partially cloudy pixels. In addition, results obtained from seven consecutive daytime and night-time NOAA-9 passes over the U.K. are presented as evidence that the scheme copes well with a variety of different situations both during the day and night.

This cloud analysis scheme has been included as one processing step of the APOLLO (AVHRR Processing Over Land cLoud and Ocean) scheme (Saunders 1987). The major impetus for developing this automated scheme was the desire to obtain both surface and cloud parameters from the AVHRR data in near real time for assimilation into an analysis for a mesoscale forecast model. This mesoscale model (Golding 1984) is currently being developed for operational use by the U.K. Meteorological Office.

2. Detection of cloud-free pixels

The overall philosophy of this cloud detection scheme is to apply up to five tests to detect cloud and then to identify a pixel as cloud-free only if *all* the tests prove negative. This does lead to the possibility that some tests will incorrectly identify some cloud-free pixels as cloud-contaminated but this is the safest way to ensure no cloud-contaminated pixels escape detection. These tests can vary depending on whether it is night or day and on the underlying surface type which is divided into three classes, sea, land and coast (i.e. mixed). The scheme uses all available channels of the AVHRR, which are in the following wavelength ranges: 0·58–0·68 μm, 0·72–1·10 μm, 3·55–3·93 μm, 10·3–11·3 μm and (for AVHRR/2) 11·5–12·5 μm for channels 1 to 5 respectively. During the day bi-directional reflectances from channels 1 and 2 and infrared brightness temperatures (i.e. equivalent black body temperatures) from

variations will mean that it is often too high or too low. Over coastal areas, however, identification of the cloud-free peak is more difficult so a fixed reflectance threshold of 15 per cent has to be used. Over sea, channel 2 reflectances are used, as they are less sensitive to aerosol and molecular scattering effects. Over the land channel 1 reflectances are used since the reflectance of land surfaces in channel 1 is much less than in channel 2, which increases the contrast between land and cloud. More details of all these tests described above can be found in Saunders (1986a).

The fourth test used during the day makes use of the ratio of near-infrared bi-directional reflectances (AVHRR channel 2) to visible bi-directional reflectances (AVHRR channel 1). Bi-directional reflectance R_n in this paper is defined as

$$R_n = \frac{G_n C + Y_n}{\cos \theta_0} \tag{1}$$

where R_n is in units of percentage reflectance, the gain G_n and intercept Y_n are given in the appendices of Lauritson *et al.* (1979), C is the raw count value received from the satellite for channel n and θ_0 is the appropriate solar zenith angle. The ratio used in the test is then simply defined as

$$Q = \frac{R_2}{R_1} \tag{2}$$

This ratio Q is close to unity over clouds, as the reflectance of clouds only decreases slightly at near-infrared wavelengths and anisotropy effects are similar in both channels and hence cancel. Over cloud-free water, however, enhanced backscattering at the shorter wavelengths due to molecular and aerosol scattering causes the visible reflectance to be often twice that in the near-infrared (outside sun glint), giving values of Q of around 0·5. Over land with growing vegetation the reflectance increases markedly at near-infrared wavelengths compared to shorter visible wavelengths (Swain and Davis 1978). Even over desert or during the winter when the vegetation is dormant the reflectance is higher at the longer wavelengths (except over snow and ice), ensuring that Q is always greater than unity. An example of typical radiance values over land, sea and cloud are shown by the histograms in figure 1. The uppermost (figure 1 (*a*)) is a histogram of visible (channel 1) reflectances. The land and sea peaks are well defined at the 'dark' end with cloudy reflectances producing a broad higher reflectance tail. The corresponding 11 μm infrared brightness temperature histogram of the same area (figure 1 (*b*)) shows the cloud-free land and sea peaks well defined and the cloud-contaminated radiances giving a cold tail to the histogram. The lower histogram (figure 1 (*c*)) is of the ratio of near-infrared to visible bi-directional reflectances (i.e. Q) over the same area. Now the cloud-free sea and land radiances are well separated with a well-defined cloudy peak close to unity. To identify cloud-free pixels a cloud-free sea or land peak is identified from the histogram of Q and then only pixels with values of Q closer to the cloud-free peak(s) than pre-defined values (0·06 over sea and 0·2 over land) are identified as cloud-free. This works well over sea but over land, as figure 1 illustrates, there is often no well-defined peak due to the large variability of the ratio over land. In this case a default threshold of 1·6 is set where all pixels with a value of Q less than this are assumed to be cloud-contaminated. If a cloud-free peak over sea cannot be identified, all pixels with values of Q greater than 0·75 are assumed to be cloud-contaminated. One problem is in areas of sun glint where Q can approach unity, having the same value as over cloud, and so the test is not applied over these areas.

The final test applied to both daytime and night-time data examines the difference

channels 4 and 5 are required for input to the scheme whereas at night the infrared brightness temperatures from channels 3, 4 and 5 are required. If channel 5 is not available, as is the case for TIROS-N and NOAA-6, -8 and -10, the scheme is simplified by omitting all tests using channel 4 and 5 differences and wherever possible substituting channel 4 for channel 5. More details of the AVHRR instrument and calibration procedure can be found in Kidwell (1985) and Lauritson *et al.* (1979). Some of the cloud detection tests have already been described elsewhere (Saunders 1986a) and so are only mentioned here briefly for the sake of completeness. However, a few improvements have been made and additional tests included, so these are described in more detail below.

The first test applied to both daytime and night-time data is an infrared threshold test using the measured AVHRR/2 12 μm brightness temperature (or 11 μm if no channel 5 is available) as a check on cloud contamination. The 12 μm brightness temperature is used because clouds have a greater optical depth at these wavelengths (Olesen and Grassl 1985). If the measured brightness temperature is below a certain threshold temperature the pixel is rejected as cloud-contaminated. A problem arises in defining an appropriate threshold temperature. Over the sea it is straightforward as the sea surface temperature (SST) varies only slowly during the year. An operational scheme could use the last 5-day mean SST for each 1 degree latitude/longitude grid point corrected for the maximum likely atmospheric absorption effects to give a brightness temperature at the top of the atmosphere. Over the land, however, the large day-to-day variability in surface temperature due to different meteorological conditions makes defining a threshold temperature more difficult. Operationally a forecast surface skin temperature could be used from a mesoscale model to define a threshold top-of-the-atmosphere brightness temperature. During the development of the scheme the thresholds were determined interactively from the data. An 11 μm brightness temperature image was displayed and the user identified cloud-free land and sea areas which were likely to be the coldest in the image. The brightness temperature over these areas were then determined and temperatures 2 deg K less than the measured values were used as threshold values. This approach is only suitable for images of small sections of one pass, as thresholds for Scotland for instance will be inappropriate over Spain. Over the coast the temperature threshold for the coldest surface (i.e. land or sea) is used, which is normally the sea during the day and the land at night.

The second test is a local uniformity or spatial coherence test applied on a 3×3 pixel array of 11 μm brightness temperatures. During the day it is only applied over the sea (with a standard deviation threshold of 0·2 deg K), as the horizontal temperature variations over cloud-free land can be considerable. We have found that the surface temperature variability over land is less at night, making a spatial coherence test possible, and so it is used with an increased standard deviation threshold of 1 deg K. The test is never applied over coastal areas where there are usually large variations in surface temperature.

The third test applied during the day (i.e. when the solar elevation is greater than 10 degrees) is a dynamic reflectance threshold test. Over land and sea a cloud-free peak can be identified in the reflectance histograms of about 50×50 pixel arrays, as shown in figure 1 (*a*), allowing a reflectance threshold to be set at a slightly higher reflectance. All pixels with reflectances above this threshold are assumed to be cloud-contaminated. Identifying a cloud-free reflectance peak and then setting a threshold value removes uncertainties due to variations in calibration and changes in surface reflectance with solar zenith/azimuth angles, etc. If a fixed reflectance threshold is applied these

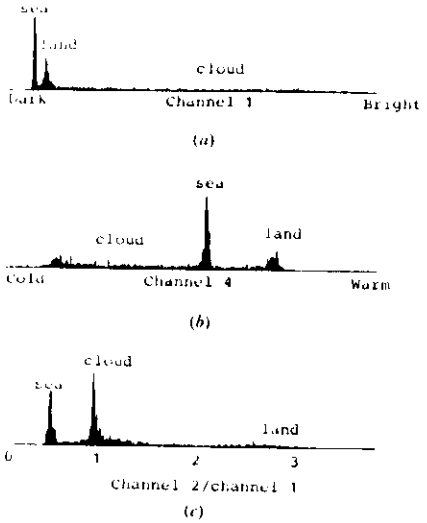

Figure 1. Histograms of NOAA-9 AVHRR data for 15 April 1985 of a 50 × 50 pixel scene over the U.K., containing clouds, cloud-free land and ocean. (*a*) Channel 1 reflectance; (*b*) channel 4 brightness temperature; (*c*) channel 2/channel 1 reflectance ratio histogram.

between the 11 μm (channel 4) and 12 μm (channel 5) brightness temperatures and for convenience this is described below along with the night-time tests. Figure 2 shows the overall flow diagram of the scheme to detect cloud-contaminated pixels during the day. A pixel must pass all of the tests described above to be assigned cloud-free. More details of the first three tests are given in Saunders (1986a).

The detection of cloud-contaminated pixels at night involves a similar series of tests but those using solar reflectances are replaced by tests which make use of the brightness temperature differences between the infrared channels (3, 4 and, if available, 5). The first two tests applied at night are the infrared threshold test followed by the local uniformity test. Both of these are also applied during the day and have already been described above.

There are a number of reasons for there being differences between the measured 3·7 μm, 11 μm and 12 μm brightness temperatures (hereafter referred to as $T_{3\cdot7}$, T_{11} and T_{12}). Firstly, brightness temperature differences between the channels would be expected even for cloud-free conditions. The total upwelling radiance at infrared wavelengths, at the top of the atmosphere for clear sky radiances at night, neglecting atmospheric scattering, is given by

$$I_\nu^{CLR} = \tau_0^H(\nu,\Psi,\theta)\varepsilon_\nu(\nu,\theta,\Phi)B_\nu(T_s) + \int_0^H B_\nu(T(h))\frac{\partial\tau_h^H(\nu,\Psi,\theta)}{\partial h}\,dh + \tau_0^H(\nu,\Psi,\theta)I_R(\nu,\Psi,\theta,\phi) \quad (3)$$

where $\tau_{h_1}^{h_2}$ is the atmospheric transmittance from height h_1 to h_2 (H is the top of the atmosphere), Ψ represents the variables defining the atmospheric state (e.g. total

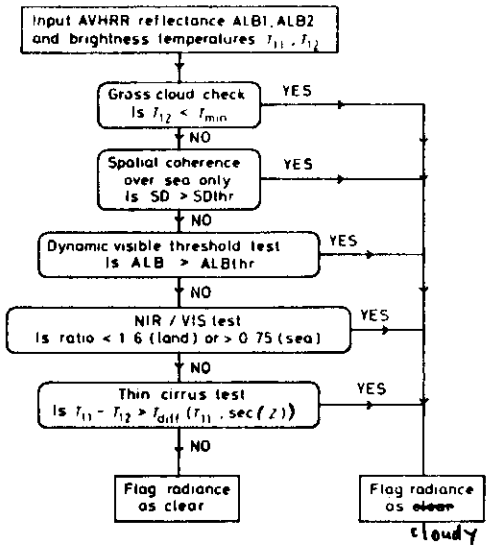

Daytime algorithm

Figure 2. Outline of the algorithm applied to AVHRR/2 data during the day to detect cloud-contaminated pixels.

column absorber amounts and broadening pressure and temperature), θ and ϕ are the satellite zenith and azimuth angles, ε_ν is the emissivity of the underlying surface, $B_\nu(T)$ is the Planck function at a frequency ν and temperature T and I_R is the downwelling atmospheric radiation, integrated over the upward hemisphere, and then reflected by the surface into the direction of the satellite sensor. The most important varying component of Ψ is the total column water vapour amount which can alter the atmospheric transmittance considerably. The first term represents the emitted surface radiance, the second is the upwelling radiance emitted by the atmosphere and the third is the downwelling atmospheric radiance reflected by the surface. The last term is small at infrared wavelengths. Both ε_ν and τ vary with frequency and so can cause differences in brightness temperature between channels. For cloud-free AVHRR data around the British Isles temperature differences of less than 1 deg K are normally observed between the three channels over both land and sea for satellite zenith angles of less than 60 degrees (Minnett 1986). In the tropics however these temperature differences are often much larger (~4 deg K) due to the higher atmospheric column water vapour amounts (Minnett *et al.* 1984).

The presence of cloud can affect the temperature differences between the channels in a number of different ways. One effect, which is easy to simulate, is that for partially filled pixels with different temperature dependence on the Planck function at different wavelengths causes a brightness temperature difference between channels. This effect is

described in more detail in the appendix of Saunders (1986a). The maximum temperature difference is obtained between the channels furthest apart in wavelength (i.e. channels 3 and 5). The second possible cause for temperature differences between channels is due to the different optical properties of cloud at the different wavelengths. For thin cloud covering the field of view, and neglecting atmospheric emission/absorption above the cloud and scattering within the cloud at infrared wavelengths, the radiance at a frequency ν is given by Platt (1975)

$$I_\nu = (1 - \varepsilon_c(\nu, \theta, \phi))I_\nu^{CLR} + \varepsilon_c(\nu, \theta, \phi)B_\nu(T_c) \qquad (4)$$

where ε_c is the emissivity of the cloud top. Variations in ε_c with frequency will lead to differences between $T_{3\cdot7}$, T_{11} and T_{12}. Cloud optical properties do vary markedly with frequency as demonstrated by Inoue (1985) and Olesen and Grassl (1985).

For thick, opaque cloud, other evidence that there can be differences in emissivity between the channels is shown by changes in the reflectivity of cloud tops at 3·7 μm but not at 11 μm or 12 μm which is caused by changes in the microphysical properties of clouds. This effect has been observed during the daytime by looking at the reflected 3·7 μm radiation from clouds (Paulus 1983, Liljas 1986, Saunders and Gray 1985, Scorer 1986). Changes in cloud top reflectivity will mean changes in emissivity which will produce significant differences between $T_{3\cdot7}$ and T_{11} or T_{12}.

The brightness temperature difference image shown in figure 3(*b*) suggests that for high and medium level cloud $T_{3\cdot7}$ is nearly always greater than T_{12}, whereas for low cloud or fog the converse is true. There can be large positive values for the $T_{3\cdot7} - T_{12}$ temperature difference (up to 21 deg K), as illustrated in the brightness temperature difference plot in figure 4(*a*), due to both partially cloud-filled pixels and thin cirrus being present. Therefore large brightness temperature differences between channels can be obtained for cloud-contaminated pixels but at mid-latitudes cloud-free pixels have small brightness temperature differences. The remaining cloud detection tests make use of this fact.

It should be emphasized that in order to obtain accurate values for differences between channels it is assumed that the radiation from the different channels originates from the same place. Allam (1986) has shown that a misregistration of about one quarter of the field of view can be observed for the AVHRR/2 on NOAA-7. Therefore a check must be made during the processing to ensure that the different channels are accurately aligned (i.e. to within 0·1 km). Any misalignments could be minimized by the method proposed by Allam (1986).

The third test applied at night determines if $T_{11} - T_{3\cdot7} > 1$ deg K, which is an effective detector of fog or low stratus. This is due to the emissivity of stratus or fog being greater at 11 μm ($\varepsilon_c = 0{\cdot}99$) than at 3·7 μm ($\varepsilon_c = 0{\cdot}8 - 0{\cdot}9$) (Bell and Wong 1981, Hunt 1973). Figure 3(*b*) shows an image of $T_{3\cdot7} - T_{12}$ brightness temperatures for part of an AVHRR pass at 02 58 GMT on 19 April 1985 which is similar to the corresponding $T_{3\cdot7} - T_{11}$ brightness temperature difference image. The dark areas (large negative values up to -6 deg K) are caused by the uniform low cloud or fog which were present at this time. A good demonstration of this effect is given by Eyre *et al.* (1984).

The fourth test consists of determining if $T_{3\cdot7} - T_{12} > 1{\cdot}5$ deg K (or $T_{3\cdot7} - T_{11} > 1{\cdot}5$ deg K if channel 5 is not available); if true then the pixel is flagged as cloud-contaminated. This will detect pixels partially filled with cloud, semi-transparent cloud and most medium and high level cloud as shown by the temperature difference image in figure 3(*b*). In addition figure 4(*a*) shows a plot of $T_{3\cdot7} - T_{12}$ versus T_{11} for pixels over

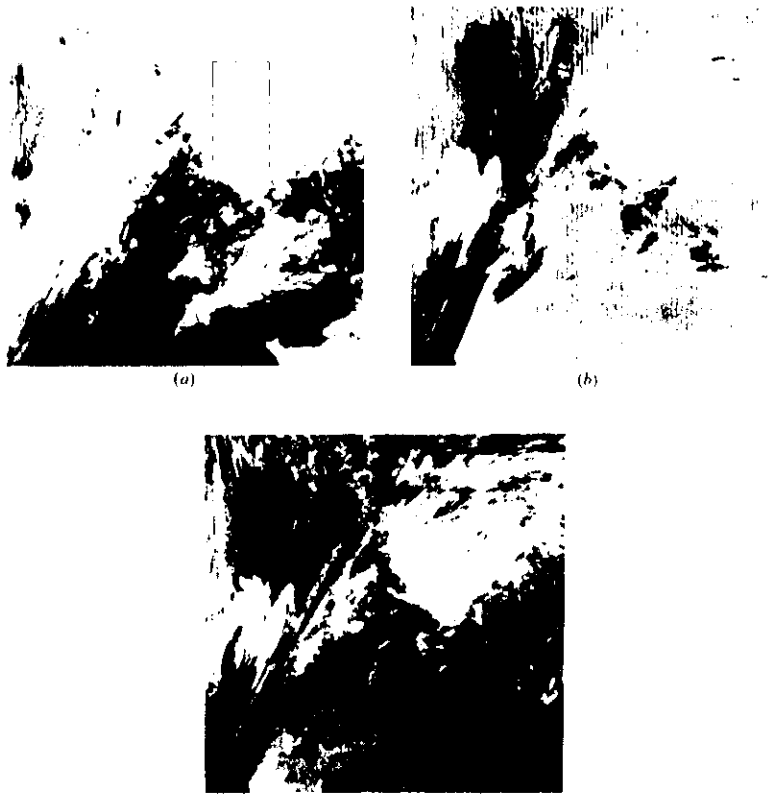

(*a*) (*b*) (*c*)

Figure 3. (*a*) AVHRR 11 μm brightness temperature image for 19 April 1985 at 02 57 GMT. Light areas represent low radiance and dark areas represent high radiance. (*b*) and (*c*) show brightness temperature difference images for $T_{3\cdot7} - T_{12}$ and $T_{11} - T_{12}$ respectively for the same image as (*a*). Dark areas correspond to negative differences and light areas to positive differences. The grey areas over the clear sea correspond to very small differences (< 0·5 deg K).

medium and high level cloud within the rectangle shown in figure 3(*a*). Almost all the pixels over this cloud have large positive values for the difference between $T_{3\cdot7}$ and T_{12}. Note however that the two effects described for these two tests can cancel, giving a brightness temperature difference close to zero. This is shown in figure 4(*a*) where all the pixels are known to be over cloud but some $T_{3\cdot7} - T_{12}$ values are still close to zero.

The final test applied to both daytime and night-time data uses temperature differences between T_{11} and T_{12}. This test can only be applied to five-channel AVHRR 2 data. Inoue (1985) shows that this temperature difference can be used to

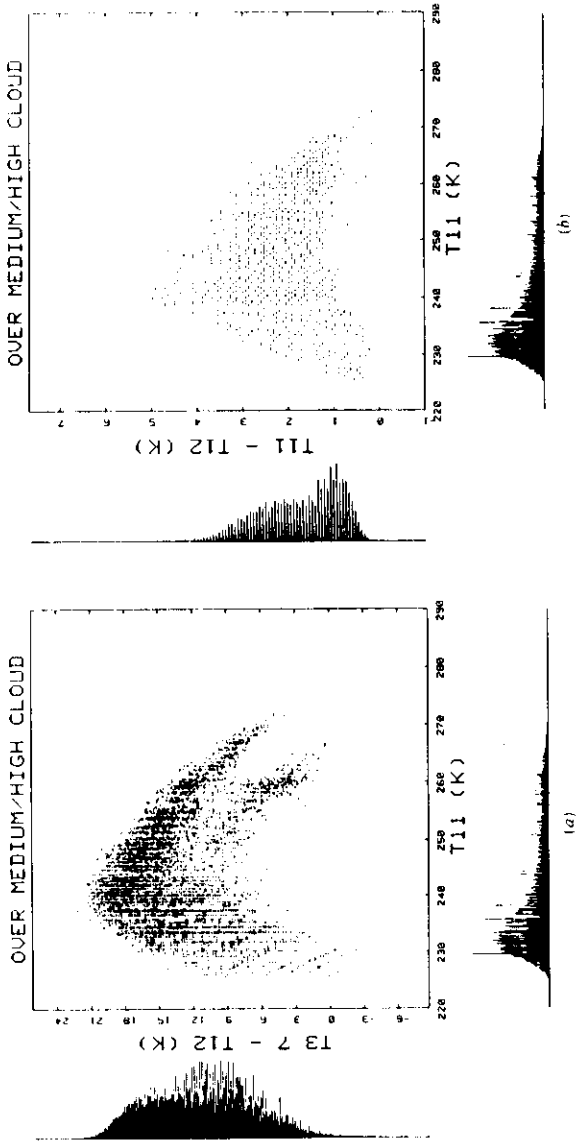

Figure 4 Bi-dimensional histograms over an area of medium high level cloud over northern England shown by the rectangle in figure 3 (*a*).
The one-dimensional histograms which make up the plots are shown along the axes.

detect semi-transparent cirrus cloud due to the different emissivities of the cloud at the two wavelengths. Roozekrans and Prangsma (1986) have also shown that this brightness temperature difference can be used to detect most types of cloud, the only exception being uniform low cloud. For pixels partially filled with optically thick high cloud the maximum temperature difference between T_{11} and T_{12} which would be expected due to the temperature dependence of the Planck function alone is only 1 deg K. However much larger temperature differences over medium and high cloud are observed in practice as shown in the brightness temperature difference image in figure 3 (*c*) and the plot in figure 4 (*b*). It is evident that brightness temperature differences of up to 6 deg K (for $T_{11} - T_{12}$) can be obtained over cloud due to the optical properties of thin cloud being different at the two wavelengths. For clear sky radiances the differences are less (often < 1 deg K) but will vary with total column water amount and satellite zenith angle θ. A set of pre-computed clear sky AVHRR brightness temperatures as used by Llewellyn-Jones *et al.* (1984) were used to show the expected dependence of $T_{11} - T_{12}$ on sec θ and T_{11} (correlated with total column water amount). Computed $T_{11} - T_{12}$ values were plotted against T_{11} and sec θ for 117 different tropical and mid-latitude maritime atmospheres selected from a data set assembled by NOAA. This does have the disadvantage that the brightness temperatures represent only maritime conditions but the differences for air masses over Western Europe would normally be small. For values of T_{11} between 260 and 310 K the maximum computed clear sky $T_{11} - T_{12}$ values were noted for these atmospheres for a range of sec θ values and a threshold value T_{diff} set at least 0·25 deg K higher than any of the computed values. Hence a look-up table was compiled of T_{diff} values for a range of values of T_{11} and sec θ. An abbreviated version of this table is given in table 1. All pixels with $T_{11} - T_{12} > T_{diff}$ are then identified as cloud-contaminated. This test is effective in detecting thin cirrus cloud and the edges of thicker cloud for both day and night.

Note that the current temperature difference thresholds used for some of the above tests are different to those given in Saunders (1986 a) in the light of experience gained after processing many more scenes. It was also found useful to vary some of the temperature difference thresholds depending on the noise level in channel 3.

A flow diagram of the overall scheme for the detection of cloud-contaminated pixels at night is shown in figure 5. It should be emphasized that although the principles of these tests apply globally the thresholds which are used are optimized for the north-west European area and may be different over other surface types (e.g. desert, snow) and for other atmospheres (e.g. tropical).

Table 1. Temperature thresholds T_{diff} in deg K for the $T_{11} - T_{12}$ cloud detection test at mid-latitudes.

	sec θ values				
T_{11} (K)	1·0	1·25	1·50	1·75	2·0
260	0·55	0·60	0·65	0·90	1·10
270	0·58	0·63	0·81	1·03	1·13
280	1·30	1·61	1·88	2·14	2·30
290	3·06	3·72	3·95	4·27	4·73
300	5·77	6·92	7·00	7·42	8·43
310	9·41	~~11·22~~ 10.34	11·03	11·60	13·39

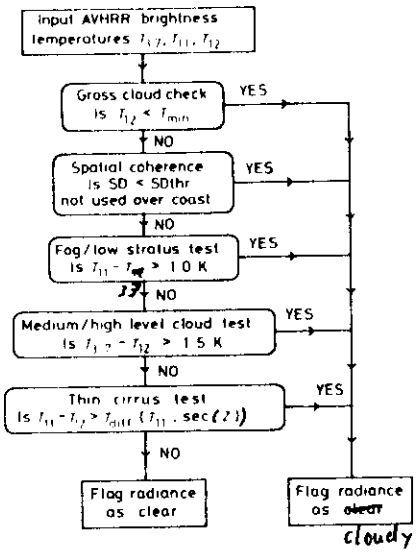

Figure 5. Outline of the algorithm applied to AVHRR/2 data during the night to detect cloud-contaminated pixels.

3. Detecting cloud-filled pixels

When detecting cloud-filled pixels, a similar approach to that for detecting cloud-free pixels is adopted. Each individual pixel is subjected to two tests to determine whether it is cloud-filled or only partially cloud covered. Different tests are employed depending on whether it is day or night, but the tests applied are the same regardless of underlying surface. They are only applied to pixels which have already been identified as cloud-contaminated by the cloud detection tests described above.

For both day and night the first test applied is a spatial coherence method over a 3 × 3 pixel array of channel 4 brightness temperatures similar to that described above for cloud detection. If there is a high standard deviation in the values for the cloud-contaminated pixels it is a reasonable assumption that the pixels are either partly cloudy or contain varying amounts of clouds at different levels. Low standard deviations indicate the array is filled with a uniform layer of cloud and correspond to the 'cold foot' of the arch in the plots of local standard deviation against brightness temperature shown by Coakley and Bretherton (1982). If the local standard deviation is greater than 1 deg K then the pixels in the array are rejected as partly cloudy. Note that pixels which are cloud-filled but have different layers of cloud within the same field of view will not be identified as cloud-filled by this test. However for deriving cloud properties it is desirable to identify pixels which are uniformly filled with only one type of cloud.

The second test applied during the day uses the histogram of channel 2:channel 1 bi-directional reflectances (i.e. Q). Unlike the conventional visible reflectance and infrared brightness temperature histograms, where the cloudy radiances produce a bright or cold tail in the histogram, the reflectance ratio histogram shows a marked peak due to cloudy pixels with values of Q close to unity as shown in figure 1 (c). The Q value of the cloud peak obtained from satellite data may vary between 0·8 and 1·1 because the reflected radiance is reduced by ozone absorption in channel 1 and by water vapour absorption in channel 2. Over low clouds therefore the ratio Q usually has lower values than over high clouds where only small amounts of water vapour are present. The position of the cloud peak is first determined 'dynamically' and then all pixels with a value of Q within 0·05 of the cloudy peak are identified as being cloud-filled. If a cloudy peak is not found in the histogram then an empirically determined value of 0·88 for the position of the cloudy peak is assumed.

At night the second test uses the differences in brightness temperature between the three infrared channels to determine if a pixel is completely cloud-filled. For low stratus or fog $T_{3.7}$ is only significantly less than T_{11} (~ 1 deg K) for pixels which are greater than 70 per cent cloud-filled (see figure 6 of Saunders (1986 a)). Therefore a threshold is set so that when $T_{11} - T_{3.7} > 1{\cdot}5$ deg K then the pixel is assumed to be cloud-filled. It is unlikely that partially cloud-filled pixels would pass this test, as for partially filled pixels $T_{3.7}$ always tends to be greater than T_{11}, cancelling out the temperature difference effect due to different cloud/fog top emissivities. The other temperature difference test applied was that only pixels with $T_{11} - T_{12} < T_{diff}$, where T_{diff} is defined in table 1, were identified as cloud-filled. This test rejects cloud edges as partially cloudy but has the disadvantage that pixels filled with thin cirrus will also be identified as partly cloudy. Hence this latter test was not applied during the day to allow pixels filled with thin cirrus to be identified as cloud-filled. Note that this implies a difference between daytime and night-time cloud-filled pixels. Another brightness temperature difference check which was attempted but found to be unsatisfactory was to reject all pixels with $T_{3.7} - T_{12} > 1$ deg K as partly cloudy. However, as figure 4(a) shows, most pixels which contain medium or high level cloud have temperature differences larger than 1 deg K even though they are apparently cloud-filled due to changes in cloud top effective emissivity between 3·7 μm and 11 μm wavelength.

The overall scheme for detecting cloud-filled radiances is shown in figure 6. Only pixels identified as cloud-filled by all tests were subsequently used for determining cloud properties (e.g. cloud top temperature, reflectance, optical depth, liquid water content).

4. Estimation of cloud cover for partially cloud-filled pixels

Having identified cloud-free and cloud-filled pixels the next step is to estimate the fractional cloud cover in the partially cloudy pixels. Cloud cover inferred from satellite radiances is really an effective cloud cover dependent on the optical properties of cloud and underlying surface at the frequency of the radiation being used. This may be quite different from the conventional cloud cover reported by a surface observer. Two different methods were adopted for inferring cloud cover, the first using only 11 μm infrared radiances for use at night, the second using visible and near-infrared radiances for use during the day. Both methods rely on the assumption that over small segments of the image the surface parameters (i.e. temperature or reflectance) remain constant. This will not be a good assumption over coastal areas and in areas where there are mixed surface types. The size of the segment chosen for this study was a fifth of a degree

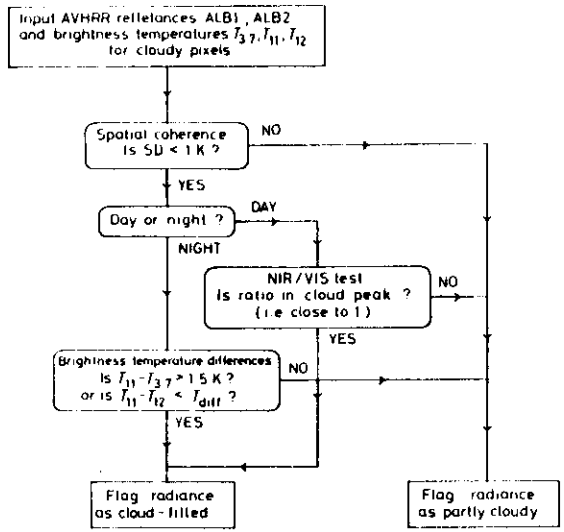

Figure 6. Outline of the algorithm applied to AVHRR/2 data to detect cloud-filled pixels.

latitude/longitude box which corresponded roughly to an area 22 km E W by 14 km N S containing about 250 pixels at 52°N.

The first method uses infrared emitted radiances to estimate an infrared fractional cloudiness N_{ir}. Note that N_{ir} is an effective cloud cover which will give the correct outgoing emitted radiance for the pixel. It is computed from the relationship

$$I_m = (1 - N_{ir})I_s + N_{ir}I_c \tag{5}$$

where I_m is the measured infrared radiance for the partially cloudy pixel, I_s is the clear sky radiance and I_c the cloud radiance. Rearranging equation (5) gives

$$N_{ir} = \frac{I_s - I_m}{I_s - I_c} \tag{6}$$

I_s is obtained by computing the mean radiance of all the cloud-free pixels and I_c from the mean radiance of all the cloud-filled pixels in the segment. Then N_{ir} is computed for each partially cloudy pixel. If there are no cloud-free pixels in the segment then a forecast surface radiance or background radiance (average of the previous few days) is taken. If there are no cloud-filled pixels then the minimum infrared radiance in the segment is taken to be a cloud-filled pixel. This latter assumption can lead to overestimates of N_{ir} if the minimum radiance in the segment is from a partially cloudy pixel, a point also made by Chou *et al.* (1986).

If we differentiate equation (6) we obtain the relationship between the uncertainty in cloud cover ΔN_{ir} and the uncertainty in measured radiance ΔI_m

$$\Delta N_{ir} = \frac{1}{1 - (I_c/I_s)} \frac{\Delta I_m}{I_s} \tag{7}$$

Note that as I_s approaches I_c the uncertainty in derived cloud cover becomes large. An example of this would be determining the coverage of low stratus cloud over the sea where the cloud top and sea surface temperatures are similar.

Because of the limitations to the infrared scheme described above, a different scheme is used during the day. The daytime scheme consists of a two-channel algorithm using both channel 1 and 2 bi-directional reflectances (i.e. R_1 and R_2 defined in equation (1)). Cloud-filled radiances are not used here; only the ratio of channel 2 to channel 1 cloud-filled reflectances defined as Q_c from equation (2) where the subscript c denotes only cloud-filled pixels were included in the average value of Q. If we rewrite equation (5) for channels 1 and 2 bi-directional reflectances in place of emitted radiances we get

$$R_{1m} = R_{1s}(1 - N_{vis}) + N_{vis}R_{1c} \tag{8}$$

$$R_{2m} = R_{2s}(1 - N_{vis}) + N_{vis}R_{2c} \tag{9}$$

and explicitly defining Q_c

$$Q_c = \frac{R_{2c}}{R_{1c}} \tag{10}$$

where N_{vis} is the effective cloud cover for reflected solar radiation, R_{nm} is the measured reflectance for a single pixel in channel n, R_{ns} is the mean clear sky reflectance and R_{nc} is the mean cloud-filled reflectance for the segment in channel n. Now we have three equations and three unknowns (R_{1c}, R_{2c} and N_{vis}), so rearranging and substituting equations (9) and (10) in (8) to solve for N_{vis} we get

$$N_{vis} = 1 - \frac{R_{2m} - Q_c R_{1m}}{R_{2s} - Q_c R_{1s}} \tag{11}$$

Values for R_{1s} and R_{2s} are obtained in the same way as for I_s described above. If there are cloud-filled pixels within the segment being considered then Q_c is derived for each cloud-filled pixel and a mean value is used in equation (11) to compute N_{vis} for each partially cloudy pixel. However if there are no cloud-filled pixels in the segment then a previously computed mean value of Q_c for another segment is used. This is a good approximation since the value of Q_c would not be expected to change much over optically thick cloud as is demonstrated by the cloud-filled peak in figure 1(*c*). Therefore with this latter method fewer errors are introduced when computing N_{vis} for segments where there are no cloud-filled pixels. One problem common to all measurements of cloud cover from reflected radiances is the uncertainty introduced by cloud shadows. Over the sea this is not a serious problem as the sea surface is often nearly as dark as the shadow and so any area of cloud shadow will be recognized as cloud-free. Over the land the reflected radiances from the shadow will be significantly less than over adjacent cloud-free land and R_{1m} and R_{2m} will be more nearly equal. This will tend to make the numerator on the right-hand term smaller and hence overestimate the cloud amount N_{vis}.

During the day equation (11) is used to compute the fractional cloud cover of partially cloudy pixels but at night equation (6) has to be used as reflectances are not available. Each pixel in the AVHRR image can now be classified as cloud-free, cloud-filled or partly cloudy and if classified as the latter a fractional cloud cover can be computed for each pixel.

5. Results

5.1. *Cloud detection scheme*

In order to assess the cloud detection scheme, full-resolution AVHRR/2 data were obtained for seven consecutive daytime and night-time NOAA-9 passes over the British Isles between 14 and 20 April 1985. These data were obtained from the satellite receiving station at the University of Dundee. The data were first Earth-located and calibrated to obtain brightness temperatures and top-of-the-atmosphere bi-directional reflectances required as input to the cloud detection scheme. The tests described in §2 were then applied to 1024 × 1024 pixel images over the British Isles extracted from the full daytime and night-time overpasses. To get an idea of the effectiveness of each test, tables 2 and 3 were compiled. These list the number and percentage of remaining cloud-

Table 2. Percentage of pixels identified as cloud-contaminated by each test for the night-time cloud detection scheme applied to a NOAA-9 1024 × 1024 pixel image over the British Isles. The percentages are of the number of pixels failing the test out of the number of clear pixels surviving after the previous test. The bottom row gives the total percentage of pixels identified as cloud-contaminated after all the tests have been applied.

	Date in April 1985 of night-time pass						
Test	14	15	16	17	18	19	20
Gross IR threshold	57	58	67	51	51	47	75
IR spatial coherence	27	12	11	22	12	10	23
Low cloud/fog $T_{11} - T_{3.7} > 1$ K	22	10	44	24	16	20	9
Mid/high cloud $T_{3.7} - T_{12} > 1.5$ K	10	10	15	27	19	4	18
Thin cirrus $T_{11} - T_{12} > T_{diff}$	7	2	9	7	2	0	2
Total percentage of pixels flagged	79	70	87	80	72	63	86

Table 3. Percentage of pixels identified as cloud-contaminated by each test for the daytime cloud detection scheme applied to a NOAA-9 1024 × 1024 pixel image over the British Isles. The percentages are of the number of pixels failing the test out of the number of clear pixels surviving after the previous test. The bottom row gives the total percentage of pixels identified as cloud-contaminated after all the tests have been applied.

	Date in April 1985 of afternoon pass						
Test	14	15	16	17	18	19	20
Gross IR threshold	69	81	77	50	40	54	59
IR spatial coherence	20	34	30	15	8	5	36
Dynamic visible threshold	6	48	21	20	15	9	11
Reflectance ratio channel 2/channel 1	16	14	14	15	14	19	15
Thin cirrus $T_{11} - T_{12} > T_{diff}$	1	2	2	1	0	1	0
Total percentage of pixels flagged	81	94	89	71	60	68	80

free pixels rejected by each test. The tests were applied in the order listed in the tables. The first thing to note is that for every pass 60 per cent or more of the AVHRR pixels were identified as cloud-contaminated, in one case rising to 94 per cent of all pixels in the image. Each test contributes significantly to the final cloud mask though some tests were more effective than others on certain days depending on the cloud types present. For instance the $T_{11} - T_{3.7}$ test detected 44 per cent of the remaining cloud-free pixels as cloud-contaminated on 16 April but only 9 per cent on 20 April. The visible threshold method similarly detected 48 per cent of the remaining pixels as cloudy on 15 April but only 6 per cent on 14 April. The last test ($T_{11} - T_{12} > T_{diff}$) rejects less pixels than earlier tests as most cloudy pixels have already been identified by previous tests. However over thin cirrus and at cloud edges it still detected cloud which the other tests had missed.

It is interesting to follow the variation in the total percentage of pixels flagged as cloud-contaminated, though note that this is not directly related to actual cloud cover. About 80 per cent of the pixels were flagged for both the night-time and afternoon overpasses on 14 April 1985. It is encouraging that they are similar as it suggests that there is no appreciable bias between the night-time and daytime schemes. On the following day however the percentage increased markedly to 94 per cent for the afternoon pass due to the presence of a warm front across the British Isles. The number of cloudy pixels remained high due to the passage of this frontal system until the afternoon of 17 April when it reduced to 71 per cent. The number of cloudy pixels had again increased by 20 April after a cold front had moved southwards across the British Isles with many large convective clouds behind it.

In order to illustrate where each test was detecting cloudy pixels and what types of cloud were detected by each method, two images were selected from the 7 days of data and the computed cloud masks overlaid on to the image. Figure 7 (*a*) shows part of a NOAA-9 early morning pass over the British Isles recorded at 02 57 GMT on 19 April 1985. Most of southern England, Wales and parts of Ireland are cloud-free. However the areas over northern England and to the west of Ireland are covered by a thick cloud layer associated with a depression centred just off north-west Scotland at that time. The overall cloud mask for this image, obtained by combining the masks from all five night-time tests, is shown as the hashed area in figure 7 (*b*) which covers 63 per cent of the pixels in the image. By inspection, there appeared to be no undetected cloud in this image. Four out of the five individual cloud masks are shown in figures 7 (*c*) (*f*). The gross infrared threshold test was omitted as this could be easily inferred by eye from the channel 4 brightness temperature image in figure 7 (*a*). The large squares apparent in the spatial coherence mask in figure 7 (*c*) are due to the coarse (50 × 50 pixel) land/sea/coast data set being used, the gaps being coastal areas where the spatial coherence test is not applied. Note that the spatial coherence test appeared to be successful over land (apart from an area of Normandy which has been incorrectly assigned as sea), but some areas which are obviously cloud have not been detected due to their uniform cloud top temperatures. The $T_{11} - T_{3.7}$ cloud mask in figure 7 (*d*) shows up many areas of fog or low cloud over the English Midlands, Essex (no... ...st of London) and off south-east Ireland which were not detected by any other test and indeed were very difficult to detect by eye in figure 7 (*a*). The surface reports at 0300 GMT bear this out with fog being reported in East Anglia, Essex and also in southern Ireland. However for the area between Birmingham and Manchester only 7 oktas of stratocumulus at around 3000 ft were reported which also shows up in this cloud mask. The $T_{3.7} - T_{12}$ cloud mask shown in figure 7 (*e*) shows that this test mainly detects

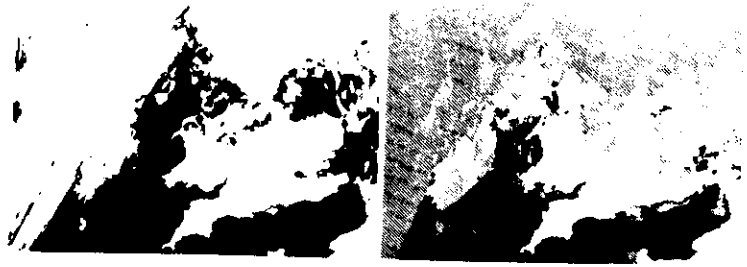

AVHRR Channel 4 image
(*a*)

Combined cloud mask over image
(*b*)

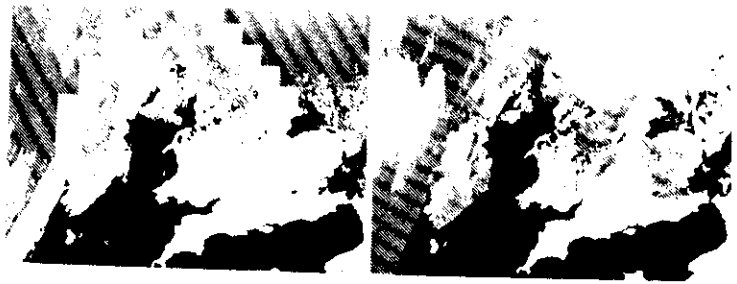

Spatial coherence test
(*c*)

Low cloud/fog test $T_{11} - T_{3.7} > 1$ K
(*d*)

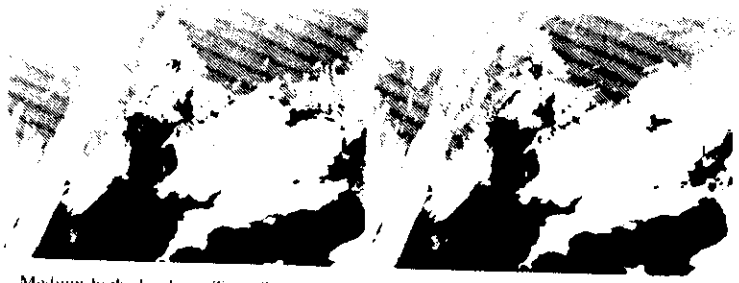

Medium high cloud test $T_{3.7} - T_{12} > 1{\cdot}5$ K
(*e*)

Thin cirrus test $T_{11} - T_{12} > T_{\text{thr}}$
(*f*)

Figure 7. An example of the combined cloud mask (*b*) (i.e. hatched areas which correspond to cloud-contaminated pixels) computed for the AVHRR image shown in (*a*) for 19 April 1985 at 02 57 GMT together with the masks produced by four of the individual cloud detection tests (*c*)–(*f*). The large square boxes which appear in (*c*) are due to those 50 × 50 pixel boxes being assigned to coast and hence no spatial coherence test is applied here.

medium and high level cloud. Finally the $T_{11} - T_{12}$ cloud mask in figure 7 (*f*) is similar to the previous cloud mask though some areas of thick high cloud are not detected by this test as is shown by the gaps in the cloud mask for the thicker clouds over Scotland.

Results for part of a daytime NOAA-9 pass recorded at 1345 GMT on 14 April 1985 are shown in figure 8. A channel 2 reflectance image is shown in figure 8 (*a*) which shows a variety of different cloud types. A band of thick high cloud lies over south-western Ireland associated with an approaching warm front. An area of thin cirrus lies ahead of this front on a line from southern Ireland to Brittany. This can barely be seen in the channel 2 reflectance image but surface reports at 1400 GMT confirm the existence of this cirrus. Over most of the land and over the sea to the west of Scotland cumulus and stratocumulus are the main cloud types. However cumulonimbus clouds are in evidence along the east coast of England, which were confirmed by surface reports. By 1800 GMT several thunderstorms were being reported over eastern England. The complete cloud mask obtained with the daytime scheme is shown in figure 8 (*b*); 81 per cent of all the pixels in the image were flagged as cloud-contaminated. The spatial coherence mask in figure 8 (*c*) again shows up the large squares due to the land/sea/coast data set but it also shows that the test detects cloud edges and small clouds well but misses some of the thicker stratocumulus south-west of Cornwall. The visible threshold mask shown in figure 8 (*d*) appears to detect all cloud types except the area of thin cirrus between southern Ireland and Brittany. The same is true of the channel 2/channel 1 mask though it did appear to be slightly better at detecting thin cirrus. Finally the $T_{11} - T_{12}$ test detects the thin cirrus cloud over the south-western approaches well and also the edges of thicker clouds.

A comparison was also carried out for this image between the cloud mask generated by the scheme described above and the results from a clustering algorithm developed by Pairman (1986). The results described by Pairman (1986) show that the cloud detection scheme somewhat overestimates the number of cloud-contaminated pixels. Over ocean 22 per cent of the pixels identified by the clustering algorithm as cloud-free ocean were identified as cloud-contaminated by the cloud detection tests. Over land the comparison is worse with 61 per cent of the cloud-free land pixels identified by the clustering algorithm assigned as cloud-contaminated by the cloud detection scheme. However Pairman (1986) states that his clustering algorithm may be grouping some sub-pixel clouds over land with the cloud-free land class, and so the clustering algorithm may be including cloud-contaminated pixels in this case.

Using a different technique, 250 pixels were picked randomly out of the image shown in figure 8 (*a*) and then each pixel manually assigned to be cloud-free land or sea, partially cloudy or a specific cloud type defined by Pairman (1986) by viewing the channel 2 reflectance and channels 3 and 4 brightness temperature images simultaneously. A cursor identified the pixel to be classified, and the images could be zoomed and enhanced interactively as desired. Values of channel 2 reflectance and the brightness temperatures in channels 3 and 4 for the pixel were also listed to help in the decision process. The results of the comparison are shown in table 4; one of the authors (RWS) and Pairman independently estimated the class for each of the 250 pixels. Again the automated scheme detected fewer cloud-free pixels with only 29 cloud-free pixels identified over sea as against 35 by both manual estimates. In fact two of the 29 pixels identified as cloud-free by the automated scheme were manually assigned to be cloud-contaminated, however both of these pixels were in a coastal area where the automated scheme is least accurate. Over land only 13 pixels were identified as cloud-free by the automated scheme whereas the manual estimates assigned 26 and 19 pixels to cloud-

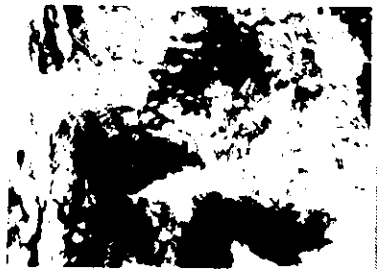

AVHRR channel 2 image
(*a*)

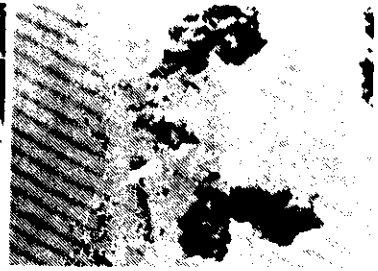

Combined cloud mask over image
(*b*)

Spatial coherence test
(*c*)

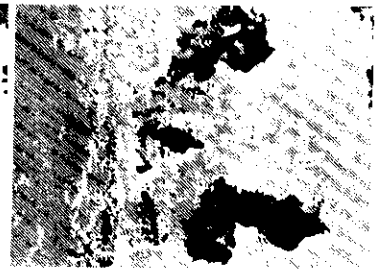

Dynamic visible threshold test
(*d*)

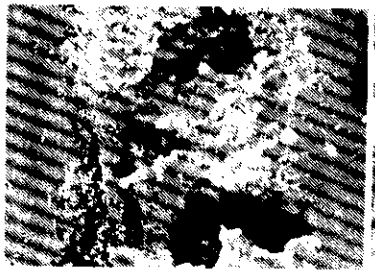

Channel 2/channel 1 test
(*e*)

$T_{11} - T_{12} > T_{\text{thr}}$
(*f*)

Figure 8. An example of the combined cloud mask (*b*) (i.e. hatched areas which correspond to cloud contaminated pixels) computed for the AVHRR image shown in (*a*) for 14 April 1985 at 1345 GMT together with the masks produced by four of the individual cloud detection tests (*c*)–(*f*). The large square boxes which appear in (*c*) are due to those 50 × 50 pixel boxes being assigned to coast or land and no spatial coherence test is applied over these surfaces.

Table 4. Comparison of manual estimates of cloud-contamination for 250 AVHRR pixels picked randomly over an image, with the automated cloud detection scheme. The number of pixels identified as cloud-free land or sea or cloud-contaminated are listed.

	Class		
	Sea	Land	Cloud-contaminated
Observer 1 Parman	35	26	189
Observer 2 Saunders	35	19	196
Automated scheme	29†	13	208

† Two of these pixels were identified as cloud-contaminated by the manual estimates but were assigned clear by the automated scheme.

free land. Note that the manual estimates were obtained using additional information (i.e. channel 3 radiances) not used in the daytime cloud detection scheme.

The automated scheme probably underestimates the number of cloud-free pixels but this is not too serious as long as all the cloud-free pixels assigned by the method are in fact cloud-free. The fact that 2 out of 250 were not shows that the scheme is not perfect, but it is encouraging that these were in coastal areas where there are known deficiencies in the scheme.

5.2. *Identification of cloud-filled pixels*

The scheme to detect cloud-filled pixels as outlined in §3 and figure 6 was applied to the same 7 days of NOAA-9 data described above. The results are shown in table 5 for both the night and day passes. The first thing to note is that the number of cloud-filled pixels in each pass identified by both tests were on average just over 20 per cent of the total number of pixels. This ranged from 57 per cent for the daytime pass on 15 April due to the warm front across the British Isles at this time to 12 per cent for the daytime pass on the 18 April when the region was cloud-free except for small cumulus clouds. All three tests were effective in detecting cloud-filled pixels as can be seen in table 5 by the different percentages detected by each test.

As an example of the detection of cloud-filled pixels during the day figure 9 shows the masks for the cloud-filled tests for the pass at 1345 GMT on 14 April 1985. The synoptic situation is described in the previous section. Figure 9 (*a*) shows the channel 2 reflectance image and figures 9 (*b*) and (*c*) the same image with the cloud-filled pixels identified by the spatial coherence test and the channel 2/channel 1 histogram test respectively. Both masks are similar, the only major differences being over the thicker frontal cloud to the south-west of Ireland where there is some vertical structure in the cloud top. Here the spatial coherence test detects only uniform cloud tops whereas the channel 2/channel 1 test detects all the cloud-filled pixels. This is also illustrated in the percentage of pixels detected by each test listed in table 5 where, with one exception, the channel 2/channel 1 test detected more cloud-filled pixels than the spatial coherence test. The mask of pixels actually assigned as cloud-filled (for pixels where both tests were successful) is shown in figure 9 (*d*). By inspection there are no obvious errors in assigning partially cloudy pixels as cloud-filled and it is encouraging that some of the

Table 5. Percentage of pixels identified as cloud filled by each test for the night-time and daytime schemes applied to NOAA-9 1024 × 1024 pixel images over the British Isles. The percentages are of the number of pixels identified by each test as cloud-filled out of the total number of pixels in the image. The final row for both day and night passes gives the percentage of pixels identified as cloud-filled after both tests have been applied, which will only consist of pixels identified as cloud-filled by both tests.

Test	Date in April 1985						
	14	15	16	17	18	19	20
Night-time pass							
IR spatial coherence							
Standard deviation < 1 deg K	30	44	54	43	36	32	40
Brightness temperature difference tests							
$T_{3.7} - T_{3.7} > 1.5$ K							
$T_{11} - T_{12} < T_{diff}$	36	26	33	19	15	28	36
Total percentage of cloud-filled pixels	22	22	28	16	13	21	26
Daytime pass							
IR spatial coherence							
Standard deviation < 1 deg K	26	65	40	32	21	21	19
Reflectance ratio channel 2/channel 1	43	74	51	30	26	35	34
Total percentage of cloud-filled pixels	22	57	30	19	12	15	13

thin cirrus over the south-west approaches is assigned as cloud-filled. These cloud-filled pixels can now be used to determine cloud properties (e.g. top temperature, reflectance, optical depth and liquid water content).

5.3. *Estimates of fractional cloud cover*

The pixels which are not identified as cloud-free or cloud-filled are assumed to be partially cloudy or filled with clouds of mixed cloud top heights. By looking at the percentages of cloud-free pixels in tables 2 and 3 and cloud-filled pixels in table 5, on average about 50 per cent of the pixels from a pass fall into this category. At present the retrieval of surface or cloud parameters is not attempted from these mixed or partially cloudy pixels. The only quantity determined for each partially cloudy pixel is fractional cloud cover as described in §4.

One interesting experiment to carry out on a daytime pass is to compare for each pixel N_{ir} computed from equation (6) with N_{vis} computed from equation (11). Figure 10 shows this comparison for a 2° × 2° area over southern England for the image shown in figure 8 (*a*) where the image was segmented into fifth of a degree latitude/longitude grid squares. The cloud reports over this area were for between 4 and 7 oktas of cumulus and stratocumulus. For each grid square a mean cloud-free and cloud-filled brightness temperature/reflectance was determined and equations (6) and (11) then applied to each pixel in the grid square. Only grid squares with more than 25 cloud-free and cloud-filled pixels, to allow an accurate estimate of clear sky and cloud-filled radiances, were included in this plot. A correlation coefficient of 0·71 was obtained betw $_{vis}$ and N_{ir}. There are a number of reasons for the scatter about the line of

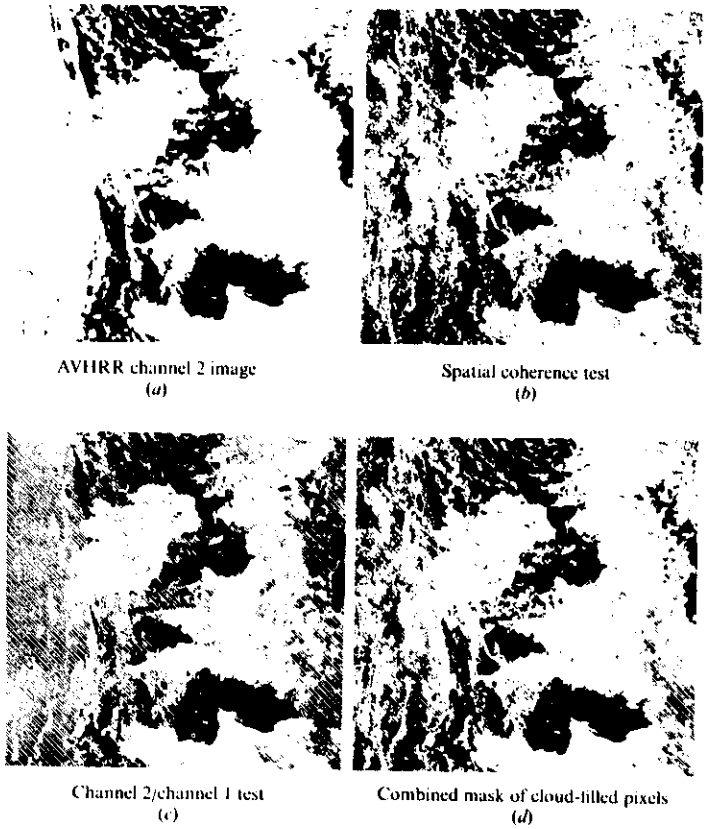

AVHRR channel 2 image (*a*)

Spatial coherence test (*b*)

Channel 2/channel 1 test (*c*)

Combined mask of cloud-filled pixels (*d*)

Figure 9. An example of the results of the tests to detect cloud-filled pixels for the AVHRR image shown in (*a*) for 14 April 1985 at 1345 GMT. The masks (i.e. hatched areas which correspond to cloud-filled pixels) from the individual tests are shown in (*b*) and (*c*) and the combined mask used to identify cloud-filled pixels is shown in (*d*).

agreement in figure 10. Firstly N_{ir} and N_{vis} are really different quantities due to the different properties of the cloud and underlying surface at the different wavelengths. Secondly the method relies on the assumption that the surface and cloud radiances are uniform over a fifth of a degree grid square which in some cases will not be valid. Finally cloud shadow effects, as discussed in §4, could lead to significant differences between N_{ir} and N_{vis}. If grid squares with no or very few cloud-filled pixels are also included then the correlation coefficient drops to 0·63, indicating that cloud-filled pixels are necessary to give representative values of N_{ir}.

Another point to note about figure 10 is that there is a suggestion that N_{vis} is not

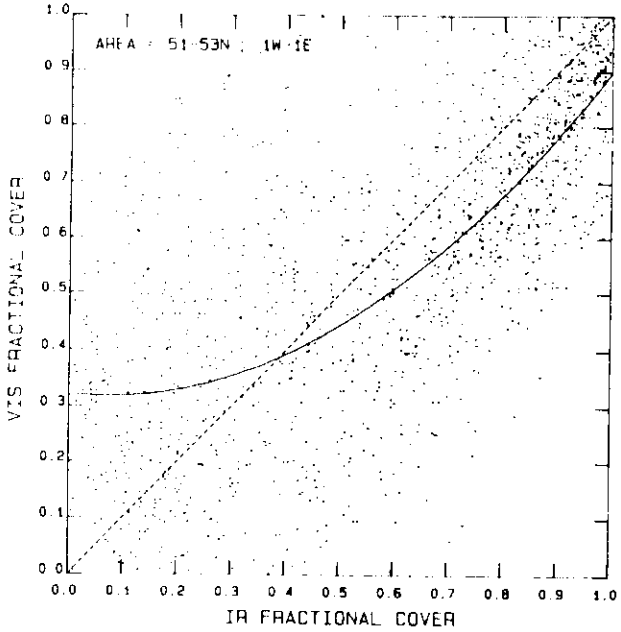

Figure 10. Comparison of N_{vis} with N_{ir} for partially cloudy pixels in a 2×2 are over southern England for the image shown in figure 8 (*a*). The curve drawn through the data is the best fit quadratic to all the points.

linearly related to N_{ir}. The best fit quadratic curve to the points, shown in figure 10, gives a variance of 0·031 for the predicted values of N_{vis} compared with the actual values. The best linear fit gives a corresponding variance of 0·033. This non-linear relationship has been shown experimentally from aircraft measurements by Kite (1987). However a more detailed study beyond the scope of this paper is required to confirm the results of Kite (1987).

Finally, as a rough validation of the mean fractional cover obtained when integrated over a fifth of a degree grid square, surface synoptic reports of cloud cover in oktas were compared with the satellite derived fractional cloudiness N_{vis}. The surface observation is always reported on the hour and was compared with the satellite measurement at the time of overpass (up to a 30 min time difference). The satellite cloud cover value was taken from the grid square which contained the surface station. Except for clear sky or complete cloud cover conditions any comparison between surface and satellite observations is inevitably subject to large errors. The satellite is measuring cloud over a well-defined fifth of a degree grid square whereas the surface observation is made over the hemisphere centred on the observing station. Also with fast moving/developing clouds, time differences of more than 10 min between observations could lead to large differences between the two types of observations.

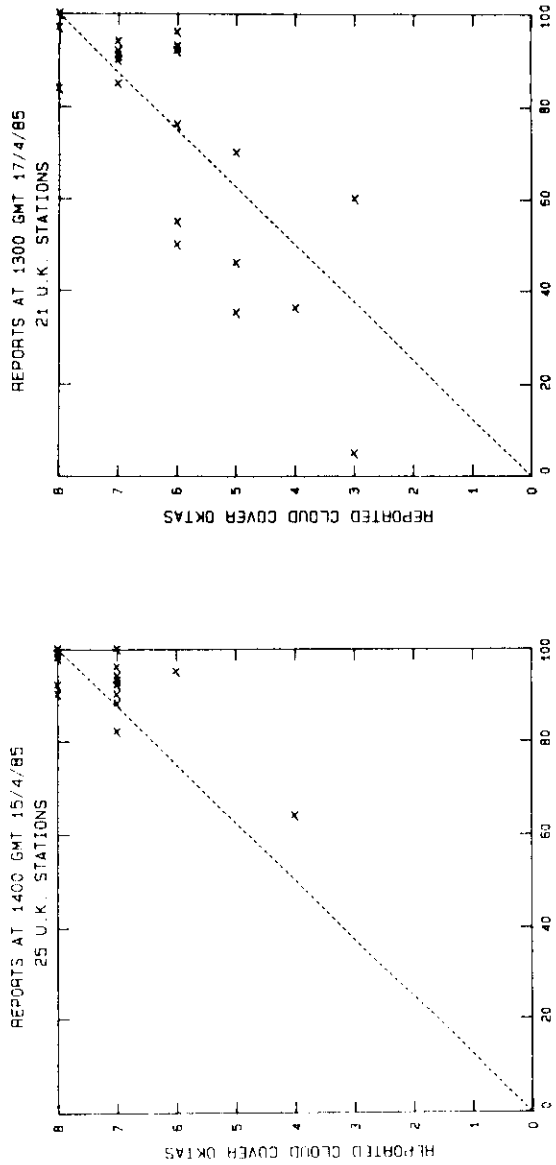

Figure 11. Comparison of surface-reported cloud cover and satellite-derived cloud cover for two NOAA-9 overpasses.

Seze *et al.* (1986) discuss these problems in more detail and in particular found a grid square of $100 \times 100\,km^2$ as giving good agreement with surface observations. The fifth of a degree grid square used here is approximately $22 \times 14\,km^2$ at 52° N. Bearing these limitations in mind, figures 11 (*a*) and (*b*) show plots of surface-reported cloud cover against satellite-derived cloud cover. Figure 11 (*a*) illustrates a case where cloud covered most of the British Isles, which reduced the inherent differences between surface and satellite observations. The agreement is reasonably good despite the small size of the grid square and the 28 min time difference between the observations. Figure 11 (*b*) is for a more broken cloudy case and here the discrepancies are bigger with the satellite measurement normally lower than the surface observation. Although this comparison is subject to large uncertainties it at least shows that the satellite-derived cloud covers are in rough agreement (1–2 oktas) with surface observations. Of course cloud cover estimates over a well-defined grid square as computed here from the satellite measurements may be a more convenient parameter to assimilate into a mesoscale model analysis than isolated surface reports of cloud cover.

6. Conclusions

An automated scheme to detect cloud-free, cloud-filled and partially cloudy AVHRR fields of view has been demonstrated using a scheme such as the one described in this paper. Different tests or thresholds have to be applied to the data depending on whether it is day or night and on the underlying surface type (i.e. land, sea or coast). It should be emphasized that this cloud detection scheme has now been applied to many AVHRR passes at different times of the year and by inspection of the cloud mask no significant amounts of cloud-contaminated pixels have escaped detection. This increases confidence in its ability to cope with different atmospheric conditions. The scheme has been successfully used to detect cloud-free AVHRR pixels to produce a 7-day mean sea surface temperature plot around the British Isles (Pescod *et al.* 1986). Also mesoscale surface and cloud parameters averaged over fifth of a degree grid squares have been derived from the AVHRR data using this scheme as a pre-processing step to define the clear sky and cloudy radiances (Saunders 1986 (*b*)). Another application using most of the cloud detection tests has been demonstrated by Lloyd (1987) and Eyre *et al.* (1986) for cloud clearing HIRS fields of view to improve the accuracy of atmospheric temperature soundings.

One component of the scheme which has not yet been fully automated is the definition of the infrared brightness temperatures over land for the infrared threshold test. When the scheme is run routinely it is intended to define the threshold temperatures over land by a forecast skin temperature from a mesoscale model.

It should be emphasized that the most difficult time of day to detect cloud is during dawn and dusk (i.e. solar elevation between $-5°$ to $+10°$). At these times the visible, near-infrared or 3·7 μm channels cannot be used reliably for cloud clearing and so only the infrared threshold test, the spatial coherence test and the $T_{11} - T_{12}$ tests are used.

One problem encountered was that, during the day, a snow-covered surface was incorrectly assigned as cloudy. The reflectance at 3·7 μm can be used to discriminate between snow/ice and cloud during the day as shown by a number of authors (Liljas 1986, Kidder and Wu 1984). Some research is now being carried out to investigate the use of the 3·7 μm channel for detecting cloud over snow/ice. In the future the inclusion of a 1·6 μm channel on the next generation AVHRR will help to alleviate this problem (Crane and Anderson 1984). It is noted that current plans suggest that NOAA will replace the 3·7 μm channel radiances with 1·6 μm channel radiances during the day and so an operational scheme using 3·7 μm reflected radiances will not be possible for all future NOAA satellites.

The scheme also identifies cloud-filled pixels successfully as judged by inspection of the original satellite images. It is hoped to carry out a more stringent validation of radiances identified as cloud-filled in the future using coincident aircraft measurements.

Finally, measurements of fractional cloud cover for individual fields of view have been derived which rely on both the cloud-free and cloud-filled radiances being correctly identified. When averaged over fifth of a degree grid squares this satellite-derived cloud cover was in most cases within 2 oktas of the surface-reported cloud cover. It is hoped to do a more comprehensive comparison of satellite-retrieved cloud cover and surface-reported cloud cover together with ISCCP-derived cloud amounts in the near future.

Acknowledgments

The authors thank Dr. J. R. Eyre and Mr. P. D. Watts of the Meteorological Office Unit, Oxford, who provided many helpful comments during the implementation of this AVHRR cloud clearing scheme, Dr. D. Pairman of the Department of Atmospheric Physics, Oxford, who compared the results of the cloud clearing scheme with his clustering algorithm, and A. Zavody of the Rutherford Appleton Laboratory who provided a data set of precomputed AVHRR brightness temperatures. The AVHRR data used in these studies were provided by the satellite receiving station at the University of Dundee, Scotland.

References

Allam, R. J., 1986, Technical note. On a slight mis-registration of AVHRR channels 3 and 4. *Int. J. remote Sensing*, **7**, 887.

Arking, A., and Childs, J. D., 1985, Extraction of cloud cover parameters from multispectral satellite measurements. *J. Climate appl. Met.*, **24**, 322.

Bell, E. J., and Wong, M. C., 1981, The near-infrared radiation received by satellites from clouds. *Mon. Weath. Rev.*, **109**, 2158.

Chou, M. D., Childs, J., and Dorian, P., 1986, Cloud cover estimation using bispectral satellite measurements. *J. Climate appl. Met.*, **25**, 1280.

Coakley, J. A., and Bretherton, F. P., 1982, Cloud cover from high resolution scanner data: detecting and allowing for partially filled fields of view. *J. geophys. Res.*, **87**, C7, 4917.

Crane, R. G., and Anderson, M. R., 1984, Satellite discrimination of snow/cloud surfaces. *Int. J. remote Sensing*, **5**, 213.

D'Entremont, R. P., 1986, Low and midlevel cloud analysis using nighttime multispectral imagery. *J. Climate appl. Met.*, **25**, 1853.

Eyre, J. R., Brownscombe, J. L., and Allam, R. J., 1984, Detection of fog at night using Advanced Very High Resolution Radiometer (AVHRR) imagery. *Met. Mag.*, **113**, 266.

Eyre, J. R., Pescod, R. W., Watts, P. D., Lloyd, P. E., Adams, W., and Allam, R. J., 1986, TOVS retrievals in the U.K.: Progress and plans. *Technical Proceedings of the 3rd International TOVS Study Conference* (Madison, Wisconsin, U.S.A., 13–19 August 1986), *CIMSS Report*, edited by W. P. Menzel. (Madison Wisconsin: CIMSS), pp. 60–91.

Eyre, J. R., and Watts, P. D., 1987, A sequential estimation approach to cloud clearing for satellite temperature sounding. *Q. Jl R. met. Soc.* (in the press).

Golding, B. W., 1984, The Meteorological Office mesoscale model: its current status. *Met. Mag.*, **113**, 288.

Hunt, G. E., 1973, Radiative properties of terrestrial clouds at visible and infrared thermal window wavelengths. *Q. Jl R. met. Soc.*, **99**, 346.

INOUE, T., 1985, On the temperature and effective emissivity determination of semi-transparent cirrus clouds by bi-spectral measurements in the 10 μm window region. *J. met. Soc Japan*, **63**, 88.

KIDDER, S. Q., and WU, H., 1984, Dramatic contrast between low clouds and snow cover in daytime 3·7 μm imagery. *Mon. Weath. Rev.*, **112**, 2345.

KIDWELL, K. B., 1985, NOAA polar orbiter data users guide. NOAA/NESDIS (Washington, D.C.: NOAA).

KIDE, A., 1987, The albedo of broken cloud fields. *Q. Jl R. met. Soc.*, **113**, 517.

KRIEBEL, K. T., 1986, Optical properties of clouds from AVHRR-2 data (Extended abstract). *Proceedings of the Sixth Conference on Atmospheric Radiation* (Williamsburg, Virginia, 13–16 May 1986) (Boston, Mass.: American Meteorological Society), p. 78.

LAURITSON, L., NELSON, G. J., and PORTO, F. W., 1979, Data extraction and calibration of TIROS-N NOAA radiometers. NOAA Technical Memo NESS 107 (Washington, D.C.: NOAA).

LILJAS, E., 1986, Use of the AVHRR 3·7 μm channel in multispectral cloud classification. SMHI Promis report No. 2.

LLEWELLYN-JONES, D. T., MINNETT, P. J., SAUNDERS, R. W., and ZAVODY, A. M., 1984, Satellite multichannel infrared measurements of sea surface temperature of the N.E. Atlantic Ocean using AVHRR/2. *Q. Jl R. met. Soc.*, **110**, 613.

LLOYD, P. E., 1987, Tropospheric sounding from the TIROS-N series of satellites. D. Phil. thesis, Department of Atmospheric Physics, Oxford University.

MCCLAIN, E. P., PICHEL, W. G., and WALTON, C. C., 1985, Comparative performance of AVHRR based multichannel sea surface temperatures. *J. geophys. Res.*, **90**, C6, 11587.

MCGINNIS, D. F., and TARPLEY, J. D., 1985, Vegetation cover mapping from NOAA/AVHRR. *Adv. Space Res.*, **5**, 359.

MINNETT, P. J., 1986, A numerical study of the effects of anomalous North Atlantic atmospheric conditions on the infrared measurement of sea surface temperature from space. *J. geophys. Res.*, **91**, 8509.

MINNETT, P. J., ZAVODY, A. M., and LLEWELLYN-JONES, D. T., 1984, Satellite measurements of sea surface temperature for climate research. *Large-Scale Oceanographic Experiments and Satellites*, edited by C. Gautier and M. Fieux (Dordrecht: Reidel), p. 57.

MINNIS, P., and HARRISON, E. F., 1984, Diurnal variability of regional cloud and clear-sky radiative parameters derived from GOES data. Part I: Analysis method. *J. Climate appl. Met.*, **23**, 993.

OLESEN, F. S., and GRASSL, H., 1985, Cloud detection and classification over oceans at night with NOAA-7. *Int. J. remote Sensing*, **6**, 1435.

PAIRMAN, D., 1986, Image processing in geophysics. D.Phil. thesis, Department of Atmospheric Physics, Oxford University.

PAULUS, R. F., 1983, On the discrimination between snow and fog in satellite pictures of high resolution. *Met. Rdsch.*, **36**, 220.

PESCOD, R. W., SAUNDERS, R. W., and EYRE, J. R., 1986, Sea surface temperature images from Advanced Very High Resolution Radiometer data. *Met. Mag.*, **115**, 318.

PHILIPIN, T., DERRIEN, M., and BRARD, A., 1983, A two dimensional histogram procedure to analyse cloud cover from NOAA satellite high resolution imagery. *J. Climate appl. Met.*, **22**, 1332.

PINKER, R. T., 1985, Determination of surface albedo from satellites. *Adv. Space Res.*, **5**, 333.

PLATT, C. M. R., 1975, Infrared emissivity of cirrus, simultaneous satellite, lidar and radiometric observations. *Q. Jl R. met. Soc.*, **101**, 119.

PRICE, J. C., 1984, Land surface temperature measurements from the split window channels of the NOAA-7 AVHRR. *J. geophys. Res.*, **89**, 7231.

REYNOLDS, D. W., and VONDER HAAR, T. H., 1977, A bispectral method for cloud parameter determination. *Mon. Weath. Rev.*, **105**, 446.

ROOZEKRANS, J. N., and PRANGSMA, G. J., 1986, Cloud clearing algorithms without AVHRR channel 3 (Abstract). Summary Proceedings of second AVHRR Users Meeting (15–16 April 1986, Rutherford Appleton Laboratory) (Chilton: Rutherford Appleton Laboratory).

ROSSOW, W. B., MOSHER, F., KINSELLA, E., ARKING, A., DESBOIS, M., HARRISON, E. F., MINNIS, P., RUPRECHT, E., SEZE, G., SIMMER, C., and SMITH, E., 1985, ISCCP algorithm intercomparison. *J. Climate appl. Met.*, **24**, 877.

SAUNDERS, R. W., 1985, Monthly mean cloudiness observed from METEOSAT-2. *J. Climate appl. Met.*, **24**, 114.

SAUNDERS, R. W., 1986a, An automated scheme for the removal of cloud contamination from AVHRR radiances over western Europe. *Int. J. remote Sensing*, **7**, 867.

SAUNDERS, R. W., 1986b, Retrieval of surface and cloud parameters from AVHRR/2 data (Extended abstract). *Proceedings of the Sixth Conference on Atmospheric Radiation* (Williamsburg, Virginia, 13–16 May 1986) (Boston: American Meteorological Society), p. 81.

SAUNDERS, R. W., 1987, A users guide to the A.P.O.L.L.O. scheme on HERMES/HOMER. Meteorological Office internal report, Met. O. 19, Branch memorandum No. 87.

SAUNDERS, R. W., and GRAY, D. E., 1985, Interesting cloud features seen by NOAA-6 3·7 μm images. *Met. Mag.*, **114**, 211.

SCHEFFER, R. A., and ROSSOW, W. B., 1983, The International Satellite Cloud Climatology Project (ISCCP). The first project of the World Climate Research Programme. *Bull. Am. met. Soc.*, **64**, 779.

SCORER, R. S., 1986, *Cloud Investigation by Satellite* (Chichester: Ellis Horwood).

SEZE, G., DRAKE, F., DESBOIS, M., and HENDERSON-SELLERS, A., 1986, Total and low cloud amounts over France and southern Britain in the summer of 1983: comparison of surface-observed and satellite-retrieved values. *Int. J. remote Sensing*, **7**, 1031.

SWAIN, P. H., and DAVIS, S. M. (editors), 1978, *Remote Sensing. The Quantitative Approach* (New York: McGraw-Hill).

Beitr. Phys. Atmosph. (August 1989) p. 165–171
0005-8173/89/0165/$07.00

Optical Properties of Clouds Derived from Fully Cloudy AVHRR Pixels

K. T. Kriebel[1], R. W. Saunders[2] and G. Gesell[3]

[1]DLR-Institut für Physik der Atmosphäre, D-8031 Oberpfaffenhofen, FRG

[2]Meteorological Office Unit, Robert-Hooke Institute for Cooperative Atmospheric Research, Clarendon Laboratory, Oxford, UK

[3]DLR-Hauptabteilung Angewandte Datentechnik, D-8031 Oberpfaffenhofen, FRG

(Manuscript received March 1989; in revised form July 1989)

Abstract

Based on a reliable identification of cloud-filled AVHRR pixels, known parametrizations of the cloud micro physics are used to connect cloud optical properties with cloud reflectance. The latter is derived from the measured radiances of the combined earth-atmosphere-cloud system. First validations of the stratus liquid water path and the cirrus optical depth by means of airborne in-situ measurements show agreement to within the expected range of uncertainty of about ± 50%. However, more validations have to be performed before the accuracy of these satellite methods can be firmly established.

Zusammenfassung

Optische Eigenschaften von Wolken, abgeleitet aus vollständig bewolkten AVHRR-Bildelementen

Basierend auf einer zuverlässigen Identifikation von total bewolkten AVHRR-Pixeln werden bekannte Parametrisierungen der Wolkenmikrophysik verwendet, um optische Eigenschaften von Wolken mit dem Wolkenreflexionsgrad zu verknüpfen. Letzterer wird abgeleitet aus der gemessenen Strahldichte des kombinierten Systems Erde-Atmosphäre-Wolke. Erste Validierungen des Flüssigwasserweges von Stratus und der optischen Dicke von Cirrus durch Flugzeugmessungen stimmen innerhalb des erwarteten Unsicherheitsbereichs von etwa ± 50% überein. Es müssen jedoch noch weitere Validierungen durchgeführt werden, bevor die Genauigkeit dieser Satellitenmethoden festgelegt werden kann.

1 Introduction

The optical properties of clouds like optical thickness and liquid or ice water path as derived from satellite data are possibly useful parameters to help validate and initialize general circulation models and limited area models of various scales. Due to improving horizontal resolution of the models, grid mesh cloudiness can be compared with satellite data, as well as optical depth and liquid or ice water path. First attempts have already been made. Sundqvist et al. (1988) use the cloud water as a prognostic variable in a mesoscale NWP model. There are several approaches to relate cloud optical properties with satellite measured radiances (e.g. Arking and Childs, 1985; Rossow et al., 1985; Platt et al., 1980; Stephens, 1978, and Starr and Cox, 1985). Using the 'AVHRR Processing scheme Over cLoud, Land and Ocean' (APOLLO) (Saunders, 1986; Saunders and Kriebel, 1988) which identifies cloud filled pixels, one can make use of parametrized schemes which relate cloud top reflectance to optical properties. We have adopted the parametrization scheme from Stephens (1978) and Stephens et al. (1984). This scheme uses a two-stream approximation of the equation of radiative transfer obtained for optically thin layers in the atmosphere developed by Coakley and Chylek (1975). It relates the cloud reflectance to the optical thickness in a simple formula which depends on only one additional variable, the backscattering coefficient. Stephens has modified the values of the backscattering coefficient to extend the applicability of this formula to water clouds with optical thicknesses up to 500. He has further shown that the optical thickness is mainly due to the liquid water path, if the drop size distribution which is a function of the liquid water path is taken into account by the various cloud models used by Stephens. He deduces simple relations between the optical thickness and the liquid water path and between the liquid water path and the upward and downward infrared emissivities. These parametrizations will apply under normal atmospheric conditions. In extreme conditions, like heavily polluted air, the relationships may have errors which exceed the ± 10 per cent given by Stephens. For ice clouds we use a relation between cloud reflectance and optical thickness given by Platt et al. (1980) and a relation between the cloud reflectance and the infrared emissivity and the ice water path given by Starr and Cox (1985).

All these parametrizations make use of the directional hemispherical reflectance of the cloud because this quantity expresses the microphysical state of the cloud in terms of upwelling radiant energy flux density, divided by the solar irradiance. However, this quantity is not directly obtained from measurements. The observable quantity is the bidirectional reflectance factor of the earth-atmosphere-cloud system at the top of the atmosphere (for nomenclature see Nicodemus, 1970, and Kriebel and Koepke, 1987). Firstly, the relationship of both reflection quantities is described. Secondly, the parametrization formulae used are given and finally first validations are presented and discussed.

2 Determination of Cloud Reflectance

Satellite instruments like the NOAA AVHRR receive an upwelling radiance determined by the instrument's field-of-view and spectral passband. After calibrating the instrument (e.g. Kidwell, 1985; Price, 1987), the radiance can be obtained and hence the bidirectional reflectance factor $R_T(\mu_o, \mu, \varphi)$ at the top of the atmosphere can be derived. The direction of incidence is given by the cosine of the solar zenith angle μ_o and the direction of observation by the cosine of the zenith angle of observation μ and the relative azimuth φ between the direction of observation and the sun. The directional-hemispherical cloud reflectance $R_c(\mu_o)$ has to be derived from $R_T(\mu_o, \mu, \varphi)$ which is required by the parametrization schemes applied. Using only fully cloudy pixels, which can be identified by the APOLLO scheme (Saunders and Kriebel, 1988), this is possible with additional information on the anisotropy, the atmospheric transmittance above the cloud, the cloud transmission properties, the angular average of $R_c(\mu_o)$ and on the surface albedo underneath the cloud.

The first step is a correction due to the anisotropy of the top-of-atmosphere reflectance which gives the directional-hemispherical reflectance:

$$R_T(\mu_o) = \frac{1}{\pi}\int_0^{2\pi}\int_0^1 R_T(\mu_o, \mu, \varphi)\,\mu\,d\mu\,d\varphi \qquad (1)$$

which is approximated by using anisotropy conversion factors $f(\mu_o, \mu, \varphi)$ computed from Nimbus 7 ERB data (Taylor and Stowe, 1984):

$$R_T(\mu_o) = R_T(\mu_o, \mu, \varphi)/f(\mu_o, \mu, \varphi) \qquad (2)$$

This anisotropy correction is based on global averages of measured radiances and distinguishes only between four cloud-free surfaces and four cloud types. Therefore it does not account for the anisotropy change with increasing optical depth. However, horizontal averaging is presumably the most important source of error if this correction is applied to pixel-size cloudiness. Using NOAA AVHRR channel 1 data (0.58–0.68 μm) only, water vapour absorption in the clouds and above the clouds can be neglected. However, an ozone correction is required to convert top-of-atmosphere reflectance $R_T(\mu_o)$ to top-of-cloud reflectance $R(\mu_o)$. The ozone transmittance in channel 1, T_{o3}, has to be applied to both the downwelling and the upwelling radiation which yields

$$\begin{aligned} R(\mu_o) &= R_T(\mu_o)/[T_{o3}(\mu_o)\,T_{o3}(\mu, \varphi)] = \\ &= R_T(\mu_o, \mu, \varphi)/[f(\mu_o, \mu, \varphi)\,T_{o3}(\mu_o)\cdot \\ &\quad T_{o3}(\overline{\mu, \varphi})] \end{aligned} \qquad (3)$$

This top-of-cloud reflectance consists of the cloud reflectance $R_c(\mu_o)$ and of the surface reflectance A_s transmitted through the cloud (e.g. Chandrasekhar, 1950):

$$R(\mu_o) = R_c(\mu_o) + \frac{A_s T_c(\mu_o)\,T_c}{1 - A_s R_c} \qquad (4)$$

Solar irradiance is diffusely transmitted downward through the cloud according to the directional-hemispherical cloud transmittance $T_c(\mu_o)$, illuminates the surface roughly isotropically and is reflected by means of the bihemispherical surface albedo A_s. This upwelling radiation is partly reflected downward at the bottom of the cloud according to the bihemispherical cloud reflectance R_c and is partly transmitted through the cloud by means of the bihemispherical cloud transmittance T_c and contributes to the directional-hemispherical reflectance at the top of the cloud, $R(\mu_o)$. The former process is accounted for by the geometric series sum formula. Now we want to replace A_s, $T_c(\mu_o)$, T_c and R_c by observable quantities and then to solve Eq. (4) for $R_c(\mu_o)$.

The relationship between the directional-hemispherical and the bihemispherical cloud reflectance can again be obtained from the Nimbus 7 ERB data. In their Figures 8 and 9, Taylor and Stowe (1984) plot the directional-hemispherical reflectance at the top of the atmosphere, $R_T(\mu_o)$, versus the solar zenith angle. The bihemispherical reflectance at the top of the atmosphere, i.e. the angular average of $R_T(\mu_o)$ with respect to μ_o, can be obtained by integrating the plotted directional-hemispherical reflectances:

$$R_T = 2\int_0^1 R_T(\mu_o)\,\mu_o\,d\mu_o \qquad (5)$$

Using R_1, a conversion factor $g(\mu_o)$ can be derived which relates R_1 to $R_1(\mu_o)$:

$$R_1 = R_1(\mu_o)/g(\mu_o) \tag{6}$$

The assumption is now that the ozone will not alter the anisotropy of the directional-hemispherical reflectance. Then, $g(\mu_o)$ can also be applied to the top-of-cloud reflectances:

$$R = 2\int_0^1 R(\mu_o)\mu_o d\mu_o = R(\mu_o)/g(\mu_o). \tag{7}$$

Because water vapour absorption in clouds is negligible below 0.75 μm (a possible aerosol absorption is neglected), the cloud transmittance can be replaced by 1 reflectance, i.e. T_c is replaced by $(1 - R_c)$ and $T_c(\mu_o)$ by $(1 - R_c(\mu_o))$. To express R_c in terms of observable quantities, Eq. (4) is integrated with respect to μ_o:

$$\int_0^1 R(\mu_o)\mu_o d\mu_o = \int_0^1 R_c(\mu_o)\mu_o d\mu_o + \frac{A_s(1 - R_c)}{1 - A_s R_c}\int_0^1 (1 - R_c(\mu_o))\mu_o d\mu_o \tag{8}$$

The term of the left hand side can be replaced by its angular mean value R/2 which is $R(\mu_o)/2g(\mu_o)$ according to Eq. (7). After rearranging we obtain

$$\frac{R(\mu_o)}{2g(\mu_o)} - \frac{A_s(1 - R_c)}{2(1 - A_s R_c)} = \int_0^1 R_c(\mu_o)\mu_o d\mu_o \left(1 - \frac{A_s(1 - R_c)}{(1 - A_s R_c)}\right) \tag{9}$$

Now $\int_0^1 R_c(\mu_o)\mu_o d\mu_o$ is substituted by its angular mean value $\frac{1}{2}R_c$ and Eq. (9) is then solved for R_c:

$$R_c = \frac{R(\mu_o) - g(\mu_o)A_s}{g(\mu_o)(1 - 2A_s) + R(\mu_o)A_s} \tag{10}$$

Equation (10) relates the angular mean cloud reflectance to observable quantities. Now Eq. (4) can be solved for $R_c(\mu_o)$ by again replacing T_c and $T_c(\mu_o)$ by $(1 - R_c)$ and $(1 - R_c(\mu_o))$, respectively and substituting R_c by Eq. (10):

$$R_c(\mu_o) = \frac{R(\mu_o)[g(\mu_o)(1 - A_s) + A_s] - g(\mu_o)A_s}{g(\mu_o)(1 - 2A_s) + R(\mu_o)A_s} \tag{11}$$

$R(\mu_o)$ is obtained from Eq. (3), $g(\mu_o)$ from the Taylor and Stowe (1984) data and the surface albedo A_s either from a-priori knowledge deduced from a look-up table derived from previous measurements or from nearest neighbour cloud-free pixels. Fixed values of A_s like 0.1 over land and 0.05 over the ocean should be used only if realistic information cannot be obtained.

3 Determination of Cloud Optical Properties

According to Stephens (1978) and Stephens et al. (1984) the directional-hemispherical cloud reflectance $R_c(\mu_o)$ is connected to the cloud optical thickness δ by

$$R_c(\mu_o) = \frac{\beta(\mu_o)\delta(\mu_o)/\mu_o}{1 + \beta(\mu_o)\delta(\mu_o)/\mu_o} \tag{12}$$

with the modified backscattering coefficient $\beta(\mu_o)$ given for water clouds with optical thicknesses from 1 to 500. From the optical thickness the cloud liquid water path LWP is obtained in gm^{-2} by

$$\log \mathrm{LWP} = (\delta \cdot 0.5454)^{0.254} \tag{13}$$

and the downward and upward infrared emissivity ϵ by

$$\epsilon\downarrow = 1 - \exp(-0.158\,\mathrm{LWP})$$
$$\epsilon\uparrow = 1 - \exp(-0.13\,\mathrm{LWP}) \tag{14}$$

Different formulae have to be applied to ice clouds. According to Platt et al. (1980), ice clouds have a higher reflectance than water clouds for the same optical thickness. The conversion factor depends on μ_o, however no complete data set is given. Therefore at present an average conversion factor of 1.6 is used to reduce the observed ice cloud reflectance to an equivalent water cloud reflectance from which the ice cloud optical thickness is derived according to Eq. (12).

To obtain ice water path and infrared emissivity, a different scheme is used given by Starr and Cox (1985). They relate the broad band albedo $\rho(\vartheta_o)$ to its particular value at the solar zenith angle $\vartheta_o = 60°$:

$$\rho(\vartheta_o) = (0.161 + 0.0117\cdot\vartheta_o + 0.386\cdot 10^{-4}\cdot\vartheta_o^2)\cdot\rho(60°) + (0.914 - 0.0152\cdot\vartheta_o)|\rho(60°)|^2 \tag{15}$$

The value at $\vartheta_o = 60°$ is related to the upward infrared emissivity $\epsilon\uparrow$:

$$\rho(60°) = 0.557\cdot\epsilon(\uparrow) + 0.105|\epsilon(\uparrow)|^2 \tag{16}$$

and the emissivity is related to the ice water path IWP:

$$\epsilon(\uparrow,\downarrow) = 1 - \exp(-k(\uparrow,\downarrow)\cdot\mathrm{IWP}) \tag{17}$$

with $k(\uparrow,\downarrow)$ the effective upward and downward broadband infrared mass absorption coefficient in

Table 1. Estimated accuracy of the liquid water path derived from APOLLO

Source of error	Estimated amount in %
Calibration	± 10
Anisotropy correction	± 20
Parametrization scheme	± 20
Horizontal inhomogeneity	± 25
Total error	± 40

$m^2 g^{-1}$. $k(\downarrow) = 0.06$ and 0.07 for nighttime and midday, respectively, and $k(\uparrow) = 0.05$. The broadband cloud albedo $\rho(\vartheta_o)$ is lower than the AVHRR channel 1 cloud reflectance $R_c(\vartheta_o)$ by a factor of 1.14 on average. This factor was derived from data given by Welch et al. (1980).

A first estimate shows that the accuracy obtained using this parameterization should not be worsen than ± 50% (Table 1).

4 First Validations

Validation of the derived cloud optical properties requires independent measurements of comparable quantities, i.e. of horizontal averages of at least the pixel size. Aircraft measurements seem to be an appropriate means provided the time necessary to obtain horizontal averages does not exceed the time difference allowed between satellite and aircraft measurement which depends on whether it is cumuliform or stratiform cloud. For stratiform cloud the time lag is believed to be less than half an hour, for cumuliform clouds it should be much less. Liquid water content (LWC) can be measured from an aircraft with a Johnson-Williams probe, CSIRO-King probe and Knollenberg PMS-probes. All three have manufacturer's calibration only, with the exception of the PMS-probe where the particle diameter read out can be adjusted. Therefore, additional user performed test procedures are absolutely necessary for obtaining reliable results for all of these probes. Because the results obtained with these devices sometimes do agree and sometimes don't (possibly depending on which drop size dominates), it is questionable which system is superior to the other or what is the real range of uncertainty. From comparisons of many flights and the requirement of consistency with other data, it is believed that the LWC can be measured to an accuracy of ± 30%. This agrees well with results from Strapp and Schemenauer (1982) who demonstrate that under favourable conditions ± 20% can be obtained. To date we have two quasi-simultaneous measurements of the LWP to validate APOLLO derived data with the vertical integral of the liquid water content (LWC) measured with a Johnson-Williams probe by means of the DLR research aircraft DO28. Time resolution of the measurements was better than one second which corresponds to a height resolution of about a metre. These data have been integrated with respect to the vertical extension of the clouds. The assumption is that each airborne LWC measurement represents the horizontal average across the range covered by the slant path. This assumption is valid in homogeneous situations.

Both comparison measurements took place on 19 January 1987 near Manching airport, 48° 42.9'N, 11° 32.1'E (Figure 1). The time difference between the satellite measurement and aircraft measurement was 30–40 minutes. Aircraft navigation is estimated to be much better than the satellite navigation due to the adjacent airport which allowed a precise location. Careful satellite navigation obtains an accuracy of better than a pixel which is less than 1 km. The horizontal projection of the slant path of the aircraft was drawn in the satellite image and the cursor defined a rectangle containing the slant path. The rectangle was set to about 15 by 10 pixels in size to cover the aircraft slant path which was around 15 km. The average LWP inside the cursor was determined by means of APOLLO and compared with the vertical integral of the LWC-profile obtained from the aircraft data. In both cases APOLLO yields lower values of the LWP than obtained from the aircraft data (see Table 2).

From Figure 1 it follows that the comparison took place with stratiform clouds with no other clouds above as was also reported from the aircraft. The visual impression of such a situation (Figure 1A) is confirmed by Figure 1B which shows warm temperatures, i.e. low clouds. The high reflectivity in channel 3 (Figure 1C) indicates water clouds (cloud-free snow pixels which could give similar data in Figures 1A and 1B are excluded by means of the snow-ice-cloud discrimination algorithm (Gesell, 1989) which is part of

Table 2. Validation of satellite derived liquid water path (LWP). Percentages indicate the deviation of the APOLLO derived LWP from the aircraft data

	Case 1	Case 2
LWP (Aircraft data) in gm^{-2}	158	104
LWP (APOLLO) in gm^{-2}	98	69
$\frac{\Delta \mathrm{LWP}}{\mathrm{LWP}_{\mathrm{aircraft}}}$ in %	39	33
$\frac{\Delta \mathrm{LWP}}{\mathrm{LWP}_{\mathrm{APOLLO}}}$ in %	64	49

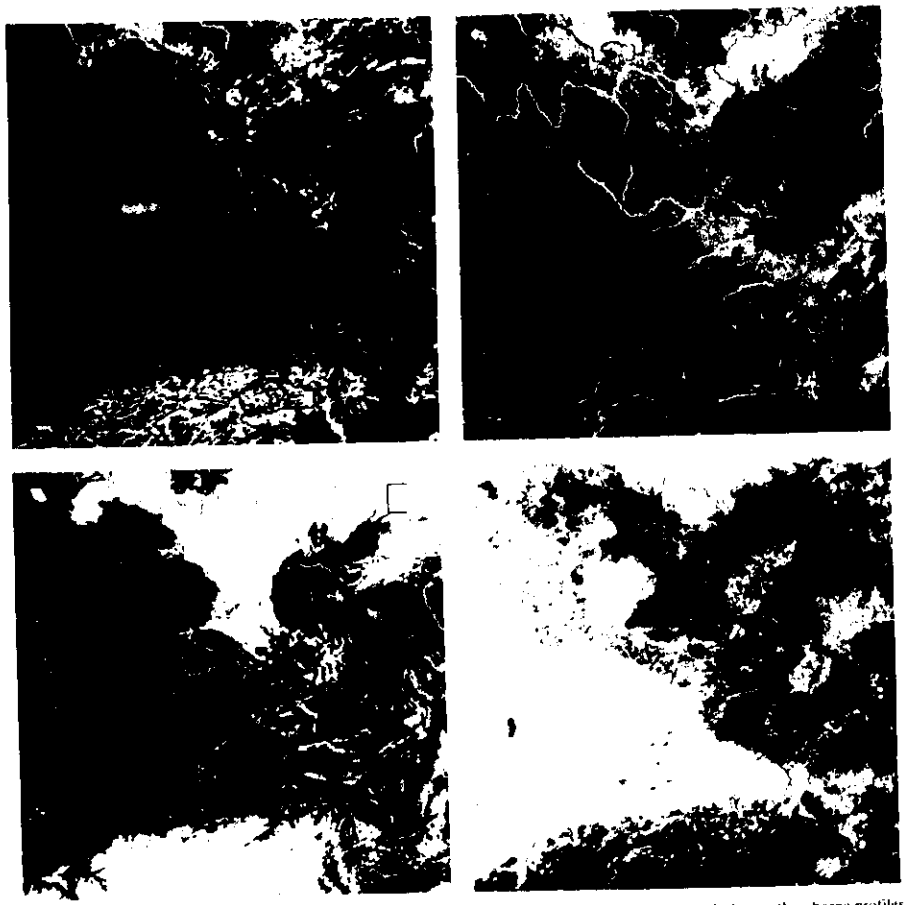

Figure 1. AVHRR images of the area in which the validation of the APOLLO derived liquid water path data with airborne profiles of the liquid water content took place on 19 January 1987. The horizontal projections of the two aircraft flight legs near Manching airport in Bavaria, FRG, are indicated as the two small straight lines in the center of each figure. In the bottom of each figure the Alps can be seen. Rivers and political boundaries are shown for orientation. The assumption of homogeneous stratiform clouds with no other clouds above, as can be concluded from the visual impression of figure 1A (channel 1) is supported by the three other figures. Figure 1B (channel 4) indicates low clouds, figure 1C (channel 3, reflected radiance only) indicates water clouds, i.e. it is not cloud-free snow, and from figure 1D (channels 4 – 5) it follows that there was no cirrus on top of the stratus.

APOLLO). Finally, from the low temperature difference between channels 4 and 5 as shown in Figure 1D it follows that no cirrus clouds can be detected above the stratus.

One possible reason for the discrepancy between aircraft and satellite LWP is horizontal inhomogeneity of the LWP as has been thoroughly investigated by Stephens (1988). However, it is not necessary to consider holes in the clouds, i.e. zero LWP, because only cloud filled pixels are used in the APOLLO scheme to derive LWP. A simple calculation shows the order of magnitude of this effect. Assume a pixel whose two halves have a different LWP. The true LWP is the arithmetic mean. AVHRR, however, measures the arithmetic mean of the reflectances produced by the two different LWP's. This mean reflectance is coupled in a different way to the true mean LWP due to the nonlinear relationship between LWP and reflectance (cf. equations 12 and 13). Assuming $\mu_0 = 1$ and $\beta = 0.07$, Table 3 shows the underestimation of the APOLLO derived LWP in terms of a factor by which the APOLLO derived LWP has to be multiplied to obtain the real LWP. This factor depends on the LWP and on the inhomogeneity. Realistic inhomogeneities are less than 3:1 in stratiform clouds (Finger and Wendling, 1990) which is equivalent to a variability of the aircraft measured LWC of ± 50% around its mean value. Curry (1986) reports somewhat higher variabilities close to the cloud top which may reflect the large vertical gradient of the liquid water content above its maximum value. This does not necessarily indicate a higher horizontal variability of the LWP than 3:1. For mixed clouds the inhomogeneity is much higher, however, per kilometer it remains in the 3:1 range (Hoffmann, 1989). This only partly explains the difference between the Johnson-Williams probe and the APOLLO parametrization. It confirms the preliminary estimation of the accuracy of APOLLO which is ± 50% in the LWP.

With cirrus clouds a first validation took place on 1 October 1987 during the first field phase of the International Cirrus Experiment (ICE). This validation compares optical depths of cirrus clouds obtained by APOLLO with airborne lidar measurements obtained from the DLR research aircraft DO228 with the ALEX-F backscattering lidar looking upward. Again the aircraft flight path was drawn in the satellite image and surrounded by a rectangular cursor. The horizontal mean of the optical depth inside the cursor box was estimated to 0.8. The lidar data were processed according to an analytical approach after Klett (Schmitz-Peiffer et al., 1989) and yielded an average optical depth of 0.73. This agreement, however, must be taken only as an indication that the parametrization used in APOLLO for ice clouds is realistic and gives the correct order of magnitude.

Table 3. Effect of horizontal inhomogeneity of LWP ($\mu_0 = 1$, $\beta = 0.07$)

Inhomogeneity	Underestimation of LWP by a factor of		
	LWP > 1000	100 < LWP < 1000	LWP < 100
9:1	2	2.33	1.61
3:1	1	1.25	1.11
1.6:1	1	1.08	1

5 Conclusions

Parametrized relations between cloud reflectance and cloud optical properties have been applied to satellite data. Emphasis has been put on the derivation of the directional-hemispherical cloud reflectance which is required by the parametrization schemes, from the measured top of the atmosphere reflected radiances. First validations against airborne in-situ measurements indicate agreement within the expected range of uncertainty. Deviations exceed the uncertainty range of the airborne measurements by about ± 25%. Besides the uncertainties connected with the parametrization schemes for homogeneous clouds, this may be due to horizontal inhomogeneities of the cloud composition. To determine the real range of uncertainty, more validations are necessary. Aircraft measurements of the LWP of arctic stratus clouds are presently being investigated to validate simultaneous satellite (NOAA AVHRR) measurements. During ICE 89 more measurements of the cirrus optical depth are expected, probably together with the first measurements of the cirrus ice water path.

Acknowledgements

The authors are indebted to J. Demmel, H. Finpel, H. E. Hoffmann, who obtained the airborne LWC data, and to P. Moerl, A. Schmitz-Peiffer, S. Schulz, who obtained the airborne optical depth data, all from DLR, Institut für Physik der Atmosphäre. We gratefully acknowledge the support of the Flight Department Oberpfaffenhofen of DLR.

References

Arking, A. and *J. D. Childs*, 1982: Retrieval of cloud cover parameters from multispectral satellite images. J. Clim. Appl. Meteor. **24**, 322–333.

Chandrasekhar, S., 1950: Radiative Transfer. Oxford: Clarendon Press. p. 393.

Coakley, J. A. and *P. Chylek*, 1975: The two-stream approximation in Radiative Transfer: Including the angle of the incident radiation. J. Atmos. Sci. **32**, 409–418.

Curry, J. A., 1986: Interactions among Turbulence, Radiation and Microphysics in Arctic Stratus Clouds. J. Atmos. Sci. **43**, 90–106.

Finger, J. E. and *P. Wendling*, 1990: Turbulence structure of arctic stratus clouds derived from measurements and calculations. Accepted for J. Atmos. Sci.

Gesell, G., 1989: An algorithm for snow and ice detection using AVHRR data: An extension to the APOLLO software package. Int. J. Remote Sens. **10**, 897–905.

Hoffmann, G.L., 1989: The horizontal and vertical structures of cloud physical parameters. Extended abstract for conference preprint volume of Fifth WMO Scientific Conference on Weather Modification and Applied Cloud Physics Beijing, China, 8–12 May 1989.

Kidwell, K. B., 1985: NOAA Polar Orbiter Data Users Guide. NOAA/NESDIS, Washington DC.

Kriebel, K. T. and *P. Koepke*, 1987: Improvements in the Shortwave Cloud-free Radiation Budget Accuracy. Part II: Experimental Study Including Mixed Surface Albedos. J. Clim. Appl. Meteor., **26**, 396–409.

Nicodemus, F. E., 1970: Reflectance nomenclature and directional reflectance and emissivity. Appl. Optics, **9**, 1474–1475.

Platt, C. M. R., D. W. Reynolds and *N. L. Abshire*, 1980: Satellite and Lidar observations of the albedo, emittance and optical depth of Cirrus compared to model calculations. Mon. Wea. Rev., **108**, 195–204.

Price, J. C., 1987: Calibration of satellite radiometers and the comparison of vegetation indices. Remote Sens. Environ., **21**, 15–27.

Rossow, W. B., F. Mosher, E. Kinsella, A. Arking, M. Desbois, E. F. Harrison, P. Minnis, E. Ruprecht, G. Seze, C. Simmer and *E. A. Smith*, 1985: ISCCP algorithm intercomparison. J. Clim. Appl. Meteor. **24**, 877–903.

Saunders, R. W., 1986: An automated scheme for the removal of cloud contamination from AVHRR radiances over western Europe. Int. J. Remote Sens., **7**, 867–886.

Saunders, R. W. and *K. T. Kriebel*, 1988: An improved method for detecting clear sky and cloudy radiances from AVHRR data. Int. J. Remote Sens., **9**, 123–150.

Schmitz-Peiffer, A., W. Renger and *P. Morl*, 1989: Fernerkundung von Cirruswolken mit einem flugzeuggetragenen Lidarsystem. Ann. Meteorol. (NF), **26**, 59–60.

Starr, D. O'C. and *S. K. Cox*, 1985: Cirrus clouds. Part I: A cirrus cloud model. J. Atmos. Sci. **42**, 2663–2681.

Stephens, G. L., 1978: Radiation profiles in extended water clouds II: Parameterization schemes. J. Atmos. Sci. **35**, 2123–2132.

Stephens, G. L., S. Ackerman and *E. A. Smith*, 1984: A Shortwave Parameterization Revised to Improve Cloud Absorption. J. Atmos. Sci. **41**, 687–690.

Stephens, G. L., 1988: Radiative Transfer through Arbitrarily Shaped Optical Media. Part I: A General Method of Solution. Part II: Group Theory and Simple Closures. J. Atmos. Sci. **45**, 1818–1848.

Strapp, J. W. and *R. S. Schemenauer*, 1982: Calibrations of Johnson-Williams Liquid Water Content Meters in a High-Speed Icing Tunnel. J. Appl. Meteor., **21**, 98–108.

Sundqvist, H., E. Berge and *J. E. Kristjansson*, 1988: Cloud Parameterisation Studies with a Mesoscale NWP Model. University of Bergen, Section of Meteorology; IBM Bergen Scientific Center, BSC 88/17, Bergen, Norway.

Taylor, V. R. and *L. L. Stowe*, 1984: Atlas of reflectance patterns for uniform earth and cloud surfaces (NIMBUS-7 ERB 61 days). NOAA Technical Report NESDIS 10.

Welch, R. M., S. K. Cox and *J. M. Davis*, 1980: Solar radiation and clouds. Meteorological Monographs **17**, No. 39, May 1980, AMS Ed., Boston, MA, USA, p. 96.

5. CONCLUSIONS